

© 2019 by Akshat Puri. All rights reserved.

MEASUREMENT OF ANGULAR AND MOMENTUM DISTRIBUTIONS OF CHARGED  
PARTICLES WITHIN AND AROUND JETS IN Pb+Pb AND  $pp$  COLLISIONS AT  
 $\sqrt{S_{NN}} = 5.02$  TeV WITH ATLAS AT THE LHC

BY

AKSHAT PURI

DISSERTATION

Submitted in partial fulfillment of the requirements  
for the degree of Doctor of Philosophy in Physics  
in the Graduate College of the  
University of Illinois at Urbana-Champaign, 2019

Urbana, Illinois

Doctoral Committee:

Professor Matthias Grosse Perdekamp, Chair  
Professor Anne Marie Sickles, Advisor  
<sup>1</sup> Professor Lance Cooper  
Professor Bryce Gadaway

# Abstract

<sup>2</sup> Studies of the fragmentation of jets into charged particles in heavy-ion collisions can help in understanding  
<sup>3</sup> the mechanism of jet quenching by the hot and dense matter created in such collisions, the quark-gluon  
<sup>4</sup> plasma. This thesis presents a measurement of the angular distribution of charged particles around the jet  
<sup>5</sup> axis as measured in Pb+Pb and  $pp$  collisions collided at a center of mass energy of  $\sqrt{s_{NN}} = 5.02$  TeV. The  
<sup>6</sup> measurement is done using the ATLAS detector at the Large Hadron Collider, and utilizes  $0.49 \text{ pb}^{-1}$  of  
<sup>7</sup> Pb+Pb and  $25 \text{ pb}^{-1}$  of  $pp$  data collected in 2015. The measurement is performed for jets reconstructed  
<sup>8</sup> with the anti- $k_t$  algorithm with radius parameter  $R = 0.4$ , and is extended to regions outside the jet cone.  
<sup>9</sup> Results are presented as a function of Pb+Pb collision centrality, and both jet and charged-particle transverse  
<sup>10</sup> momenta. It was observed that in Pb+Pb collisions there is a broadening of the jet for charged particles with  
<sup>11</sup>  $p_T < 4 \text{ GeV}$ , along with a narrowing for charged particles with  $p_T > 4 \text{ GeV}$ . Ratios between the angular  
<sup>12</sup> distributions in Pb+Pb and  $pp$  showed an enhancement for particles with  $p_T < 4 \text{ GeV}$  in Pb+Pb collisions,  
<sup>13</sup> with the enhancement increasing up to 2 for  $r < 0.3$ , and remaining constant for  $0.3 < r < 0.6$ . Charged  
<sup>14</sup> particles with  $p_T > 4 \text{ GeV}$  show a small enhancement in the jet core for  $r < 0.05$ , with a growing suppression  
<sup>15</sup> of up to 0.5 for  $r < 0.3$  in Pb+Pb collisions. The depletion remains constant for  $0.3 < r < 0.6$ .

*For my Mother, Father, and Brother*

# Contents

18	<b>Chapter 1 Introduction</b>	1
19		
20	<b>Chapter 2 Theoretical Introduction</b>	3
21	2.1 Quantum Chromodynamics	3
22	2.2 Heavy Ion Collisions	6
23	2.3 Quark Gluon Plasma	11
24	2.4 Jets and Jet Quenching	13
25	2.4.1 Jet Reconstruction	17
26	<b>Chapter 3 Major Jet Measurements</b>	21
27	3.1 Dijet Balance: $x_J$	21
28	3.2 Modification of jet yields: $R_{AA}$	22
29	3.3 Jet Fragmentation	25
30	3.4 Effective Quenching	25
31	3.5 Jet Fluid model	29
32	3.6 Hybrid Model	33
33	<b>Chapter 4 Experimental Setup</b>	35
34	4.1 The Large Hadron Collider	35
35	4.2 The ATLAS Detector	37
36	4.2.1 Inner Detector	37
37	4.2.2 Calorimeter	39
38	4.2.3 Muon Spectrometer	41
39	4.2.4 Other subsystems	41

# Chapter 1

## Introduction

40 The Large Hadron Collider (LHC) at the European Center for Nuclear Research (CERN), is one of the worlds  
41 most expensive and complicated machines. It was built with the purpose of accelerating subatomic particles  
42 to close to the speed of light and colliding them to study their underlying structure. Detectors around the  
43 LHC ring, the biggest of which are ATLAS (A Toroidal LHC ApparatuS), CMS (Compact Muon Solenoid),  
44 ALICE (A Large Ion-Collider Experiment), and LHCb (LHC-Beauty), study these collisions and use the  
45 debris as a playground to verify and expand the "Standard Model" of particle physics. This thesis will focus  
46 on measurements of collisions involving heavy ions as measured by the ATLAS detector.

47 Relativistic heavy ion collisions such as those at the LHC provide insight into the interactions between  
48 quarks and gluons. These fundamental building blocks of all matter interact via the strong force, the  
49 theoretical framework of which is described by Quantum Chromodynamics (QCD). This theory dictates  
50 that quarks and gluons are confined, i.e. locked together to form composite particles and cannot exist  
51 independently, making their study extremely difficult. Relativistic heavy ion collisions provide an extreme  
52 environment where nuclear matter can "melt" and form a deconfined medium that consists of free quarks  
53 and gluons. This state of matter, called the Quark Gluon Plasma (QGP) is what existed a few microseconds  
54 after the Big Bang, and is what eventually cooled and expanded to form the existing universe. It

55 The quark-gluon plasma (see Refs. [1, 2] for recent reviews) can be probed by jets, sprays of particles that  
56 come from hard scattering processes between the nucleons involved in the collision. These jets are produced  
57 early in the collision and interact with the QGP as they make their way to the detector. Studying the rates  
58 and characteristics of these jets in Pb+Pb collisions, and comparing them to similar quantities in  $pp$  collisions  
59 can provide information on the properties of the QGP. In particular, studying the fragmentation pattern of  
60 these jets and how the energy is distributed around the jet axis can provide more information on the jet  
61 structure and put constraints on the medium response to the jet.

62 This thesis is split into 4 main chapters. Chapter 2 briefly describes the general theoretical background  
63 on QCD, heavy ion collisions, QGP, and jets, giving context to the measurements discussed in this thesis.  
64 Chapter 3 will briefly discuss major jet measurements done by the ATLAS Heavy Ion Group. Chapter 4

65 gives an overview of the LHC and the ATLAS detector. Chapter ?? will describe the work undertaken to  
66 become a member of the ATLAS Collaboration, and Chapter ?? will provide a detailed description of the  
67 measurement to determine the angular distributions of charged particles in Pb+Pb and  $pp$  collisions.

# Chapter 2

## Theoretical Introduction

68 This section shall discuss the theoretical background necessary to understand jet measurements. It will  
69 discuss the fundamentals of quantum chromodynamics (QCD), the heavy ion collision system and the quark  
70 gluon plasma that is formed, and finally jets and jet energy loss.

### 71 2.1 Quantum Chromodynamics

72 Quantum Chromodynamics is a gauge theory with SU(3) symmetry that describes the dynamics of the strong  
73 interactions between quarks and gluons. It is part of the Standard Model [3], the building blocks of which  
74 are shown in Figure 2.1.

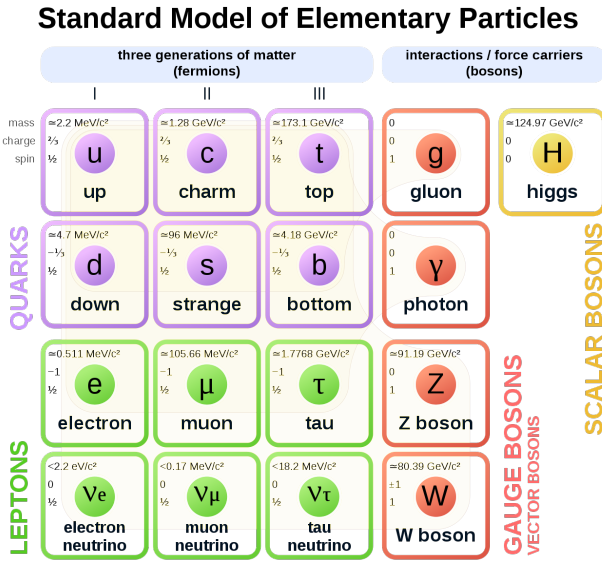


Figure 2.1: The elementary particles of the standard model.

75 Quarks are fermions with a spin of 1/2, and carry a fractional electric charge as well as a color charge.  
76 They all have mass and come in six flavors: up, down, top, bottom, strange, charm. The lightest quarks

77 (u and d) combine and form stable particles, while the heavier quarks can only be produced in energetic  
 78 environments and decay rapidly. Gluons are gauge bosons (force carriers) with a spin of 1, and are what hold  
 79 quarks together. The dynamics of the quarks and gluons are described by the QCD Lagrangian given as [4]:

$$\mathcal{L}_{\text{QCD}} = \sum_q \bar{\psi}_{q,a} (i\gamma^\mu \partial_\mu \delta_{ab} - g_s \gamma^\mu t_{ab}^C \mathcal{A}_\mu^C - m_q \delta_{ab}) \psi_{q,b} - \frac{1}{4} F_{\mu\nu}^A F^{A\mu\nu} \quad (2.1)$$

80 where  $\psi_{q,a}$  and  $\psi_{q,b}$  are quark-filled spinors for a quarks with flavor  $q$ , mass  $m_q$ , and color  $a$  and  $b$  respectively,  
 81 with the values for  $a$  and  $b$  ranging from 1 to 3 (for the three colors). The  $\mathcal{A}_\mu^C$  corresponds to the gluon field  
 82 with  $C$  taking values from 1 through 8 (for the 8 types of gluons). The  $t_{ab}^C$  corresponds to the Gell-Mann  
 83 matrices that are the generators of the SU(3) group, and dictate the rotation of the quarks color in SU(3)  
 84 space when it interacts with a gluon. The coupling constant is encoded within  $g_s$ , which is defined by  
 85  $g_s \equiv \sqrt{4\pi\alpha_s}$ . The field tensor  $F_{\mu\nu}^A$  can be written in terms of the structure constants of the SU(3) group  
 86  $f_{ABC}$ , and is given by:

$$F_{\mu\nu}^A = \partial_\mu \mathcal{A}_\nu^A - \partial_\nu \mathcal{A}_\mu^A - g_s f_{ABC} \mathcal{A}^B \mathcal{A}^C \quad (2.2)$$

87 While many parallels can be drawn between Quantum Electrodynamics (QED, the theory that describes  
 88 photons and electrons) and QCD, the difference between the two comes from the gluon-gluon interactions  
 89 allowed in QCD, making it non-Abelian. These interactions can be summarized as shown in Figure 2.2.

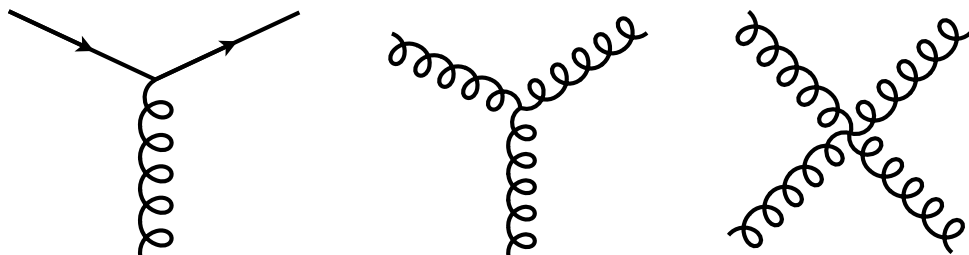


Figure 2.2: The allowed vertices in QCD. The vertices involving two or more gluons are unique to QCD and do not have a QED analog.

90 A core feature of QCD is that the coupling constant  $\alpha_s$  has an energy dependence shown in Figure 2.3.  
 91 This dependence can be expressed in terms of the  $\beta$  function as

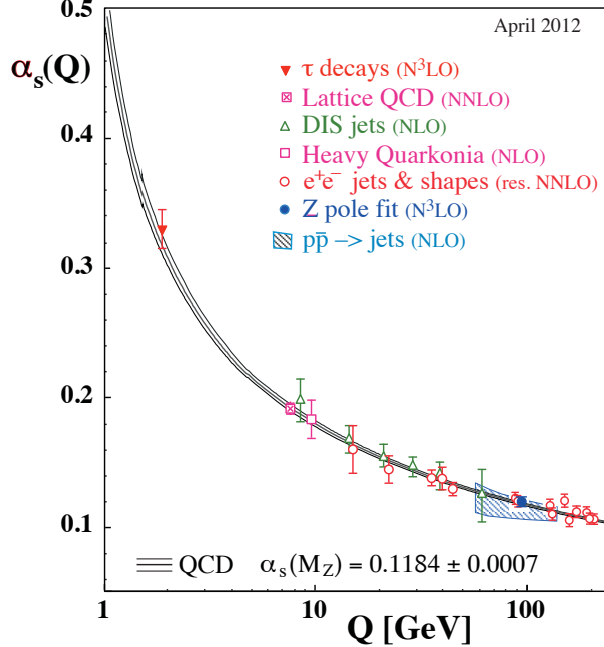


Figure 2.3: The running coupling constant  $\alpha_s$  as a function of the momentum transfer  $Q$ . Figure taken from Ref. [4].

$$Q^2 \frac{\partial \alpha_s(Q^2)}{\partial Q^2} = \beta(\alpha_s(Q^2)) \quad (2.3)$$

where  $Q$  is the momentum transfer in the particle reaction. The beta function can be expressed using perturbative QCD (pQCD) as

$$\beta(\alpha_s) = -(b_0 \alpha_s^2 + b_1 \alpha_s^3 + b_2 \alpha_s^4 \dots) \quad (2.4)$$

where the coefficients  $b_i$  depend on the number of colors and flavors.

This running coupling constant is small and asymptotically tends to zero at large energy scales (or at small distances) and is large at small energy scales (large distances). This running coupling phenomenon leads to two key behaviors: asymptotic freedom and color confinement.

**Asymptotic Freedom:** At high energy scales (small distances), the QCD coupling constant  $\alpha_s$  is small and tends to zero, implying a free particle behavior of quarks and gluons. This has been observed by a

100 variety of deep inelastic experiments [5–18]

101 **Color Confinement** The opposite end of the running coupling constant phenomenon is color confinement.  
102 This property of QCD forbids the direct observation of free quarks and gluons, allowing only for  
103 composite particles that are color singlets.

104

## 105 2.2 Heavy Ion Collisions

106 Heavy ion collisions can be used as a tool to study the Quark Gluon Plasma [19] . They provide access to  
107 the otherwise confined partons, and give insight into the QCD phase diagram and the transition between the  
108 QGP and hadronic matter.

109 In a heavy ion collision, the colliding nuclei are accelerated to relativistic energies and are Lorentz  
110 contracted discs. In the case of a Pb+Pb collision the relativistic  $\gamma$  factor is between 100 and 2500 for  
111 beam rapidities of  $y = 5.3$  and  $8.5$ . Each nucleus contains many colored quarks and antiquarks, with three  
112 more quarks than anti-quarks per nucleon, with the  $q\bar{q}$  popping in and out of the vacuum due to quantum  
113 fluctuations. These  $q\bar{q}$  pairs are sources of transverse color fields and the corresponding force carriers, the  
114 gluons.

115 When these pancake like discs collide, their color fields interact and there is a color charge exchange,  
116 producing longitudinal color fields that fill the space between the receding discs. While the maximum energy  
117 density in the process occurs just at the collision, the energy density 1 fm/c after the collision is  $12 \text{ GeV/fm}^3$ ,  
118 much higher than the  $500 \text{ MeV/fm}^3$  in a typical hadron. Lattice QCD calculations in thermodynamics show  
119 that at these energies, the partons produced in the collision cannot be treated as a collection of distinct  
120 hadrons.

121 After the collision the energy density between the receding nuclei starts to decrease as the QGP cools and  
122 expands. This process, seen in Figure 2.4, continues till the energy density drops to below that within a  
123 hadron and the fluid “hadronizes”. These individual hadrons briefly scatter off of each other before they  
124 freely fly towards the detector (freeze-out).

125 While Figure 2.4 shows snapshots of a head on (central) collision between two large nuclei, it is possible to  
126 have collisions where the impact parameter is larger and hence the overlap region is smaller. These collisions,  
127 called peripheral collisions, qualitatively undergo the same process described above, with the size and shape  
128 of the QGP being different.

129 The basic parameters of a heavy ion collision such as the number of participants  $N_{\text{part}}$  and number of

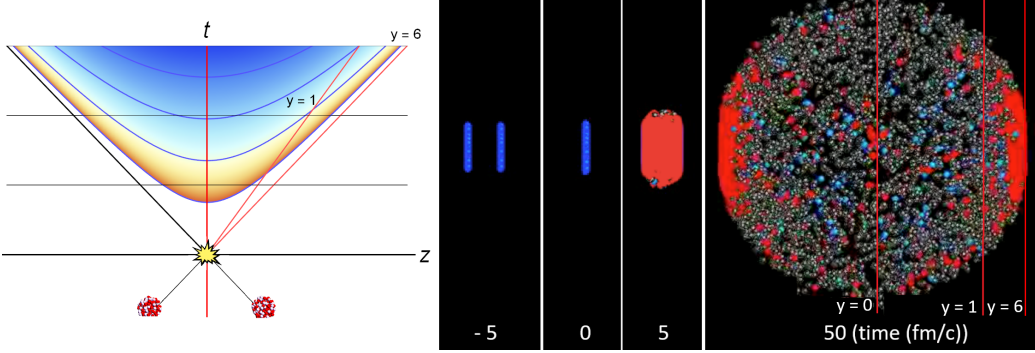


Figure 2.4: (left) Space-time diagram for a heavy ion collision. The color is indicative of the temperature of the QGP formed. (right) Snapshots of a heavy ion collision at  $\sqrt{s_{NN}} = 2.76$  TeV at different times. The Lorentz contracted nuclei are in blue while the QGP is in red. Figure from Reference [2].

binary collisions  $N_{\text{coll}}$  can be determined using the Glauber Monte Carlo simulations [20, 21]. This technique considers a nucleus-nucleus collision as a collection of independent binary nucleon-nucleon collisions; the colliding nuclei are modeled as a set of uncorrelated nucleons being positioned within the nucleus based on a the nuclear density function uniform in azimuthal and in polar angles. The nuclear density function shown in Figure 2.5 for Au and Cu, is given by:

$$\rho(r) = \rho_0 \frac{1 + w(r/R)^2}{1 + e^{\frac{r-R}{a}}} \quad (2.5)$$

where  $\rho_0$  is the nucleon density,  $R$  is the nuclear radius,  $a$  is the skin depth,  $w$  corresponds to deviations from a circular shape and is typically zero for larger nuclei like Cu, W, Au, Pb, and U. For the Pb nuclei used at the LHC,  $w = 0$ ,  $R = 6.62$  fm and  $a = 0.55$  fm [22].

They are then arranged with a random impact parameter  $b$  based on the distribution  $d\sigma/db = 2\pi b$  and projected onto the  $x - y$  plane as shown in Figure 2.6. They are then made to travel on straight trajectories, colliding if  $d \leq \sqrt{\sigma_{\text{inel}}^{\text{NN}}/\pi}$ , where  $d$  is the distance between the nucleons in a plane transverse to the beam axis and  $\sigma_{\text{inel}}^{\text{NN}}$  is the inelastic scattering cross section. [23, 24]

An important parameter for colliding nuclei A and B with  $A$  and  $B$  nucleons is the thickness function  $T_{AB}$ . It describes the effective overlap area in which specific nucleons in the two colliding nuclei can interact. It can be defined in terms of the probability per unit area of a given nucleon being located at a particular distance  $s$  within the nucleus. For the colliding nuclei A and B, this is given by  $T_A(\mathbf{s}) = \int \rho_A(\mathbf{s}, z_A) dz_A$  and  $T_B(\mathbf{s}) = \int \rho_B(\mathbf{s}, z_B) dz_B$ . Then,  $T_{AB}$  is given by

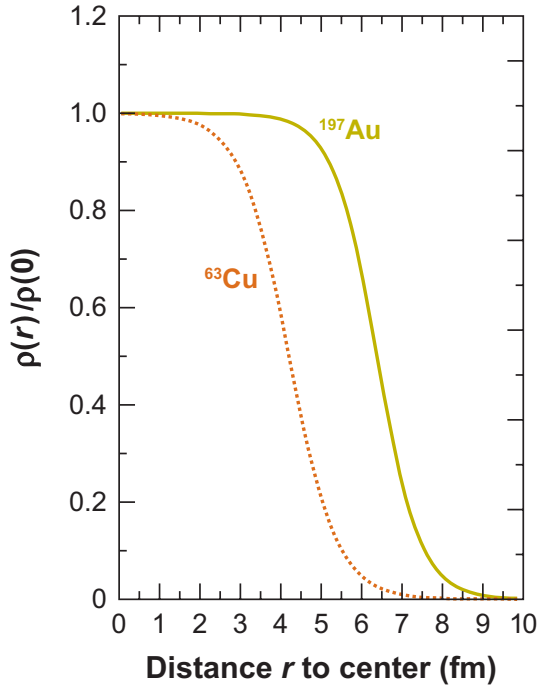


Figure 2.5: The nuclear density distributions for nuclei used at RHIC: Cu ( $w = 0$ ,  $R = 4.2$  fm and  $a = 0.48$  fm) and Au ( $w = 0$ ,  $R = 6.38$  fm and  $a = 0.535$  fm) [22, 23].

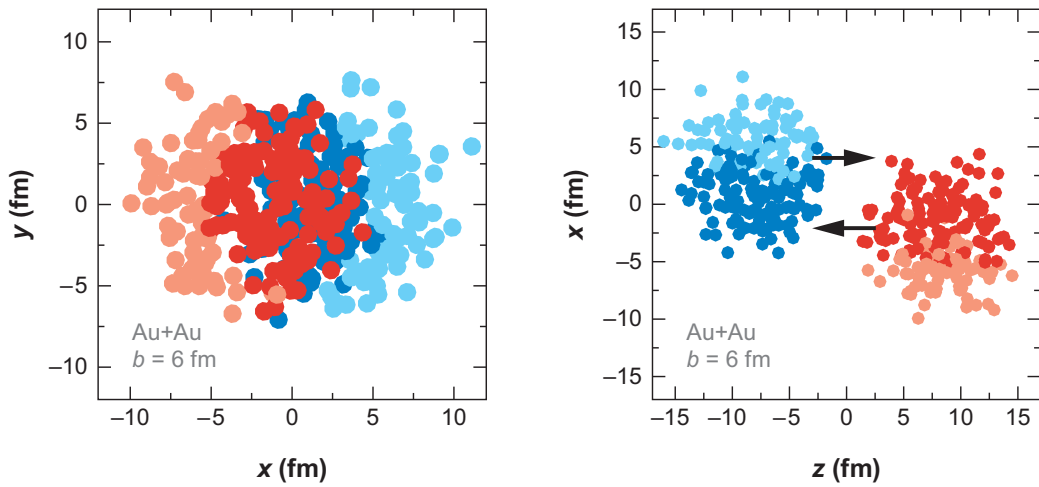


Figure 2.6: A Glauber Monte Carlo event for  $\text{Au} + \text{Au}$  at  $\sqrt{s_{\text{NN}}} = 200$  GeV with impact parameter of 6 fm viewed in the (left) transverse plane and (right) along the beam axis. Darker circles represent the participating nucleons. Taken from [23].

$$T_{AB}(\mathbf{b}) = \int T_A(\mathbf{s})T_B(\mathbf{s} - \mathbf{b})d^2s \quad (2.6)$$

147 The probability of then having  $n$  interactions between nuclei  $A$  and  $B$  is given by the binomial distribution:

$$P(n, \mathbf{b}) = \binom{AB}{n} \left[ T_{AB}(\mathbf{b})\sigma_{\text{inel}}^{\text{NN}} \right]^n \left[ 1 - T_{AB}(\mathbf{b})\sigma_{\text{inel}}^{\text{NN}} \right]^{AB-n} \quad (2.7)$$

148 where the first term is the number of combinations for finding  $n$  collisions from  $AB$  possibilities, the  
149 second term is the probability for having exactly  $n$  collisions, and the last term the probability of  $AB - n$   
150 misses. Then the total probability of an interaction between A and B is

$$\frac{d^2\sigma_{\text{inel}}^{\text{AB}}}{db^2} \equiv p_{\text{inel}}^{\text{AB}}(b) = \sum_{n=1}^{AB} P(n, \mathbf{b}) = 1 - \left[ 1 - T_{AB}(\mathbf{b})\sigma_{\text{inel}}^{\text{NN}} \right]^{AB} \quad (2.8)$$

151 Then the total cross section is given by

$$\sigma_{\text{inel}}^{\text{AB}} = \int_0^\infty 2\pi b db \left[ 1 - \left( 1 - T_{AB}(\mathbf{b})\sigma_{\text{inel}}^{\text{NN}} \right)^{AB} \right] \quad (2.9)$$

152 and  $N_{\text{coll}}$  and  $N_{\text{part}}$  are given by [25, 26]

$$N_{\text{coll}}(b) = \sum_{n=1}^{AB} n P(n, b) = AB \times T_{AB}(b)\sigma_{\text{inel}}^{\text{NN}} \quad (2.10)$$

$$N_{\text{part}}(b) = A \int T_A(\mathbf{s}) \left[ 1 - \left( 1 - T_B(\mathbf{s} - \mathbf{b})\sigma_{\text{inel}}^{\text{NN}} \right)^B \right] d^2s + B \int T_B(\mathbf{s} - \mathbf{b}) \left[ 1 - \left( 1 - T_A(\mathbf{s})\sigma_{\text{inel}}^{\text{NN}} \right)^A \right] d^2s \quad (2.11)$$

153 The correlation between  $N_{\text{coll}}$  and  $N_{\text{part}}$  can be seen in Figure 2.7

154 The charged particle multiplicity  $N_{\text{ch}}$  along with the combination of  $N_{\text{part}}$  and impact parameter  $b$  can  
155 be used to determine the centrality of a heavy ion event. An example of this is shown in Figure 2.8.

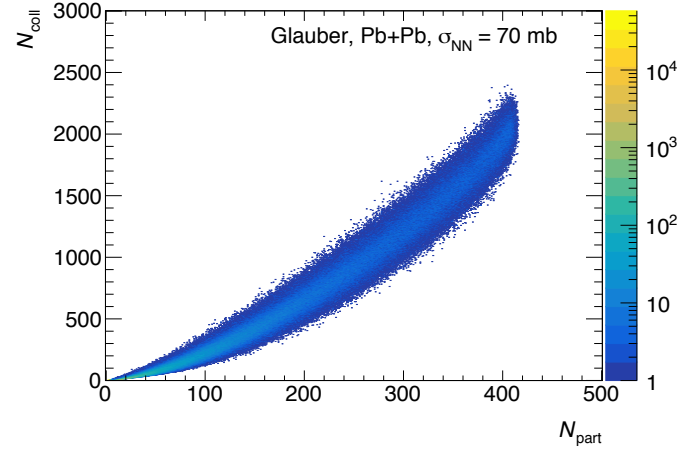


Figure 2.7: The  $N_{\text{coll}} - N_{\text{part}}$  correlation for Pb+Pb collisions at  $\sqrt{s_{\text{NN}}} = 5.02 \text{ TeV}$ . Taken from [27].

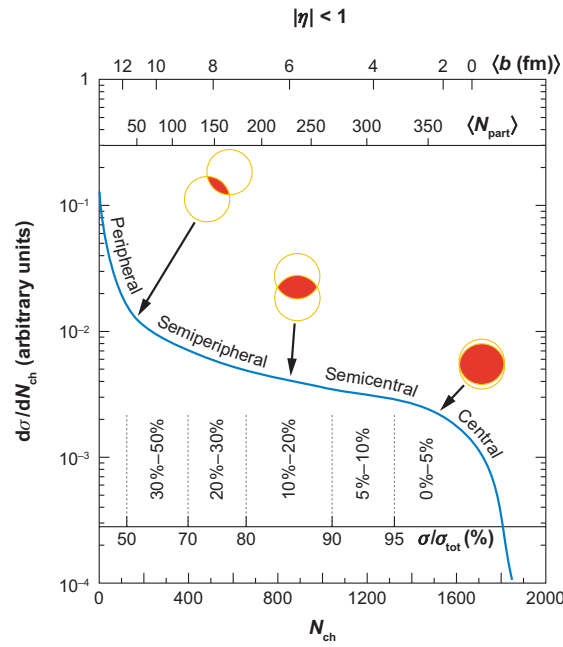


Figure 2.8: The correlation between the observable  $N_{\text{ch}}$  and  $N_{\text{part}}$  to determine the centrality distribution. Taken from [23].

## 156 2.3 Quark Gluon Plasma

157 Extreme conditions of temperature and pressure like those in relativistic heavy ion collisions lead to the  
 158 formation of the Quark Gluon Plasma [19]. It is believed to have filled the early universe a few microseconds  
 159 after the Big Bang and might be present in the cores of extremely compact objects like neutron stars [28,  
 160 29]. The phase transition between the free quarks and gluons within the QGP and the confined quarks and  
 161 gluons within hadrons can be seen in Figure 2.9.

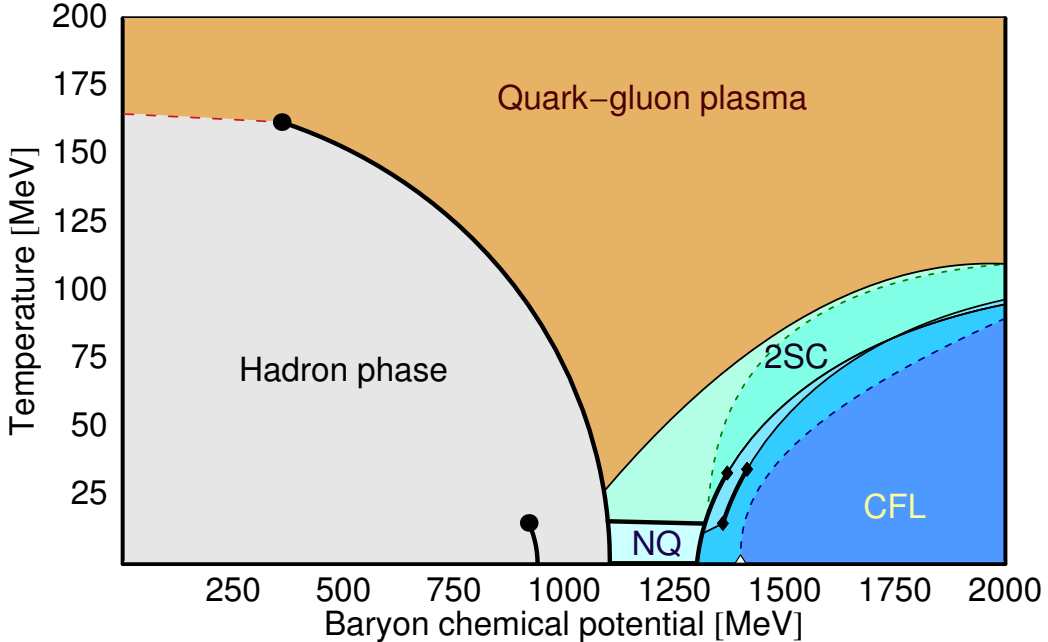


Figure 2.9: The QCD phase diagram of nuclear matter. Figure from Reference [30].

162 This state of matter exists for 1–10 fm/c, depending on the collision energy, above  $\lambda_{\text{QCD}} = 200$  MeV, the  
 163 fundamental energy scale in QCD. Thermal photons from the QGP reveal that it reaches temperatures of  
 164 300–600 MeV in central collisions at 200 GeV [31] and 2.76 TeV [32], showing very little collision energy  
 165 dependence. Further, the chemical freeze-out temperature was found to be 160 MeV via measurements of  
 166 ratios of final state hadrons containing the light  $u, d$  quarks [33–35] with the thermal freeze-out being 100–150  
 167 MeV [36–39]. These measurements paint a picture of the QGP being formed early in the heavy ion collision.  
 168 It has a non-uniform energy density and temperature determined by the 'colliding nuclei and collision energy.  
 169 The QGP then cools and expands as described by relativistic hydrodynamics, and as its temperature falls  
 170 below 160 MeV, it experiences a crossover phase transition and hadronizes. This system continues to cool  
 171 and expand, until at 95 GeV there is a thermal freeze-out.

172 The QGP was initially thought to be a weakly coupled parton gas because of asymptotic freedom from

173 QCD. The highly energetic collisions such as those at the LHC would imply a weak interaction between the  
 174 quarks and gluons that make up the plasma. This would result in rare scatterings between the constituents  
 175 of the gas and wash out any spatial anisotropies based on the collision geometry. On the other hand, a  
 176 strong coupling within the QGP would result in the pressure gradients in the medium being driven by  
 177 hydrodynamics and spatial anisotropies would be transformed to momentum anisotropies in the particles  
 178 produced as shown in Figure 2.10. In this picture, the non-uniform structure of the colliding nuclei would  
 179 cause a momentum anisotropy that would be further enhanced when looking at collisions that are less central  
 180 and do not have perfect overlap between the colliding nuclei. These observations were seen in azimuthal  
 181 correlation measurements implying that the medium is indeed strongly coupled [40–43].

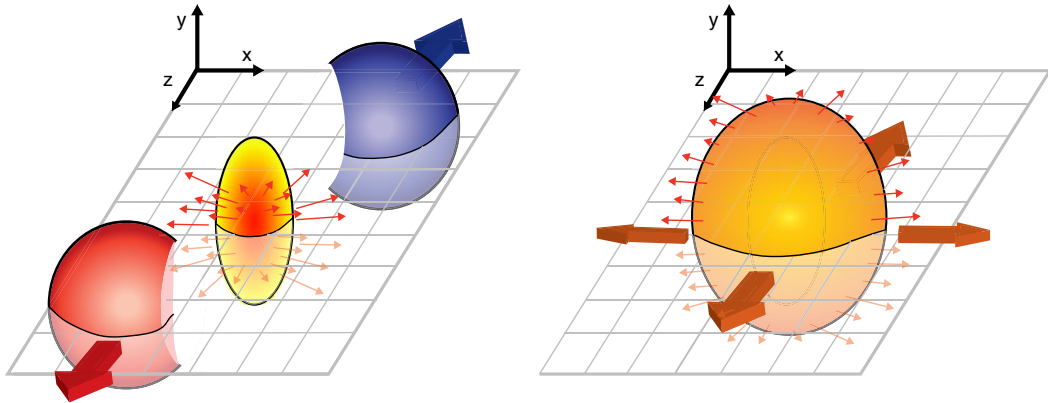


Figure 2.10: Schematic diagrams of the initial overlap region (left) and the final spatial anisotropy generated (right). Taken from [44].

182 A Fourier Transform of the angular distribution of charged hadrons in the collision debris can quantify  
 183 these momentum anisotropies and give the anisotropic flow coefficients  $v_n$ , defined as [45]:

$$\frac{d\bar{N}}{d\phi} = \frac{\bar{N}}{2\pi} \left( 1 + 2 \sum_{n=1}^{\infty} v_n \cos(n(\phi - \bar{\Psi}_n)) \right) \quad (2.12)$$

184 where  $\phi$  is the angle in the transverse plane,  $\bar{\Psi}_n$  are the event plane angles, and  $\bar{N}$  is the average number  
 185 of particles per event. Some of these coefficients are shown in Figure 2.11. The measured anisotropies can be  
 186 used to constrain the specific viscosity given by the ratio of viscosity to entropy density,  $\eta/s$ , and have shown  
 187 that the QGP has a  $\eta/s$  of near the theoretical minimum of  $1/4\pi$  [46].

188 The Bjorken energy density of the QGP can be derived using [49]:

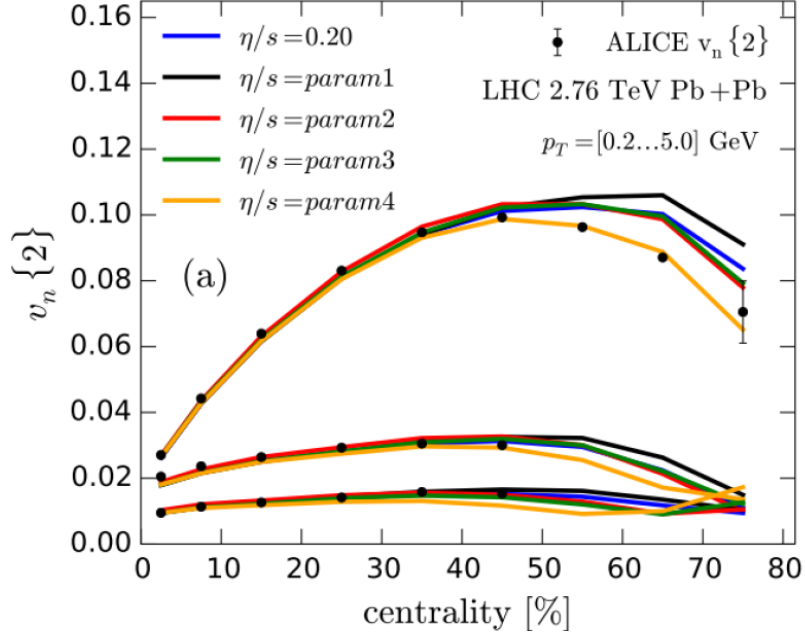


Figure 2.11: Comparison of a hydrodynamic model from [47] to anisotropy measurements by ALICE [48] for different parameterizations of  $\eta/s$  and for different  $v_n$ ,  $n = 2, 3, 4$  from top to bottom, as a function of collision centrality.

$$\varepsilon \geq \frac{dE_{\text{T}}/d\eta}{\tau_0 \pi R^2} = \frac{3}{2} \langle E_{\text{T}}/N \rangle \frac{dN_{\text{ch}}/d\eta}{\tau_0 \pi R^2} \quad (2.13)$$

where  $dN_{\text{ch}}/d\eta$  is the number of charged particles produced per unity pseudorapidity,  $dE_{\text{T}}/d\eta$  is the transverse energy per unit pseudorapidity,  $\tau_0$  is the thermalization time,  $R$  is the nuclear radius, and  $E_{\text{T}}/N \approx 1$  GeV is the transverse energy per emitted particle. As shown in Figure 2.12, the energy density at the LHC was measured to be approximately  $15 \text{ GeV/fm}^3$ , much higher than the values measured at RHIC [50, 51].

## 2.4 Jets and Jet Quenching

Hard scatterings in particle collisions result in the production of highly energetic partons that form conical sprays of hadrons called jets. A schematic of this process is shown in Figure 2.13. Jet production in a vacuum is well described in context of perturbative QCD [53] where processes involving large momentum transfers like high  $p_{\text{T}}$  hadron production can be described in terms of the parton distribution functions, scattering cross sections, and final state fragmentation functions as shown below [54]:

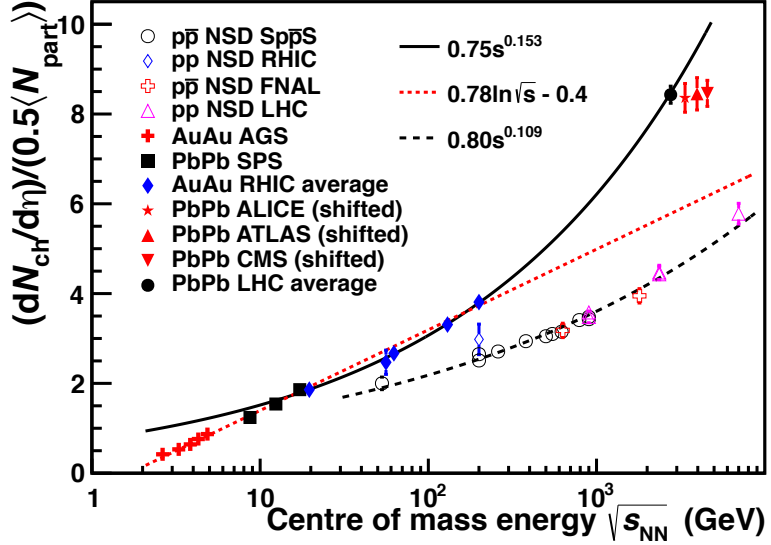


Figure 2.12:  $dN_{\text{ch}}/d\eta$  per colliding nucleon pair as a function of collision energy in  $pp$  and nucleus-nucleus collisions [52].

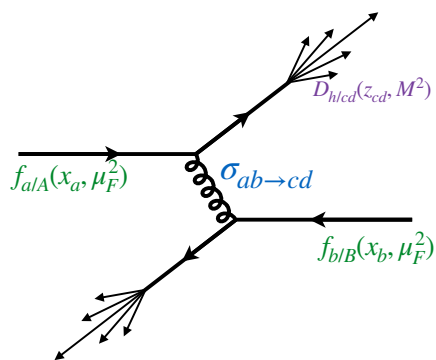


Figure 2.13: Jet production from the process  $pp \rightarrow hX$ , factorizing in terms of the parton distribution functions, scattering cross sections, and jet fragmentation functions. [54]

$$\begin{aligned}
d\sigma_{pp \rightarrow hX} &\approx \sum_{abjd} \int dx_a \int dx_b \int dz_j f_{a/p}(x_a, \mu_f) \otimes f_{b/p}(x_b, \mu_f) \\
&\otimes d\sigma_{ab \rightarrow jd}(\mu_f, \mu_F, \mu_R) \\
&\otimes D_{j \rightarrow h}(z_j, \mu_f)
\end{aligned} \tag{2.14}$$

where  $x_a = p_a/P_A, x_b = p_b/P_b$  are the initial momentum fractions carried by the interacting partons,  $z_j = p_h/p_j$  is the momentum fraction carried by the final observed hadron.  $f_{a/p}(x_a, \mu_f)$  and  $f_{b/p}(x_b, \mu_f)$  are the two parton distribution functions (PDFs),  $d\sigma_{ab \rightarrow jd}(\mu_f, \mu_F, \mu_R)$  is the differential cross section for parton scattering and  $D_{j \rightarrow h}(z_j, \mu_f)$  is the fragmentation function (FFs) for parton  $j$  to hadron  $h$ .  $\mu_f$  and  $\mu_F$  are the factorization scales and  $\mu_R$  is the renormalization scale, and are typically taken to be the same hard scale  $Q$ . The PDFs characterize the initial state and represent the probability of finding a parton with momentum fraction  $x$  (shown in Figure 2.14) in the initial hadron, while the FFs describe the probability of fragmenting to a hadron  $h$  with given kinematic properties.

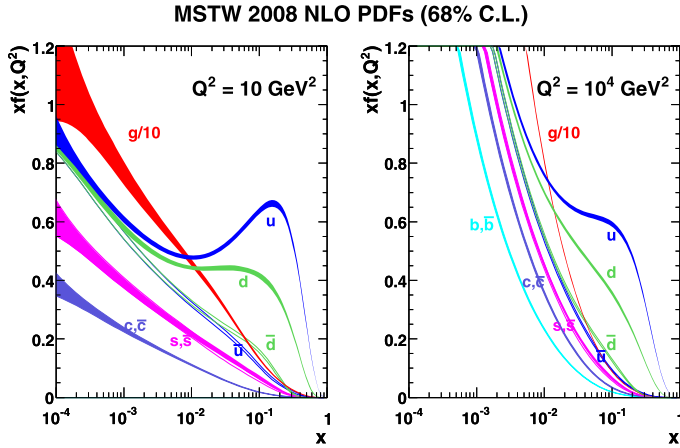


Figure 2.14: The next to leading order (NLO) PDFs at (left)  $Q^2 = 10 \text{ GeV}^2$  and (right)  $Q^2 = 10^4 \text{ GeV}^2$ . The band is the associated one-sigma (68%) confidence level uncertainty. Taken from [55]

In the case of heavy ion collisions, the jet observables can be modified due to two sources: the nuclear PDF being distinct from a proton PDF, and the formation of the quark gluon plasma. The former is collectively referred to as cold nuclear matter (CNM) effect, and can be quantified by defining a nuclear modification factor for the PDF:

$$R_a^A(x, Q^2) = \frac{f_{a/A}(x, Q^2)}{f_{a/p}(x, Q^2)} \quad (2.15)$$

where  $f_{a/A}$  and  $f_{a/p}$  are the nuclear and proton PDFs respectively. This  $R_a^A$  factor is determined by global fits to data from DIS measurements [56–58]. CNM effects include the following contributions:

- Shadowing: This is a destructive interference effect that reduces the interactions of a nucleon incident on a nucleus within its interior and on its back face. This effect reduces the effective number of nucleons in an inelastic interaction to  $A^{2/3}$ . For  $Q^2$  of the order of a few  $\text{GeV}^2$ , this effect dominates for  $x < 0.05$  and implies  $R_a^A(x, Q^2) < 1$  [59].
- Anti-shadowing: This compensates for the shadowing effect based on the momentum sum rule, and for  $Q^2$  of the order of a few  $\text{GeV}^2$  implies  $R_a^A(x, Q^2) > 1$  over the region  $0.05 < x < 0.20$ .
- EMC: The modification of the nuclear structure function was first observed by the European Muon Collaboration [60]. Recent observations have suggested that the effect is caused by short-range correlated nucleon pairs within nuclei [61]. For  $Q^2$  of the order of a few  $\text{GeV}^2$ , this effect dominates for  $0.2 < x < 0.80$  and implies  $R_a^A(x, Q^2) < 1$ .
- Fermi Motion: This effect considers the motion of the nucleons within the nucleus. It results in  $R_a^A(x, Q^2) > 1$  over the  $x > 0.8$  region for  $Q^2$  of the order of a few  $\text{GeV}^2$  [62].

Cold nuclear matter effects are experimentally measured using  $p + A$  systems where the size and shape of the plasma, and hence any effects thereof, are a lot smaller.

The second source of modification is the formation of the hot and dense quark gluon plasma. The hot nuclear matter effects further serve as an independent confirmation that the medium formed is strongly interacting. Jets are formed early enough that they traverse the Quark Gluon Plasma and as strongly interacting particles, are both affected by, and affect the QGP. This interaction typically results in the jet losing energy and forward momentum [63, 64], with the lost energy being deposited in the medium [65]. Jets can also pick up momentum transverse to the parton direction [66]. The hot nuclear matter effects can be considered to be a combination of collisional and radiative energy losses summarized in Figure 2.15.

- Collisional energy loss: This is a combination of elastic and inelastic collisions of the hard parton with the constituents of the quark gluon plasma.
- Radiative energy loss: This is the larger source of parton energy loss and jet quenching. These are modified by the presence of the plasma due to scatterings off of the plasma constituents. A variety of

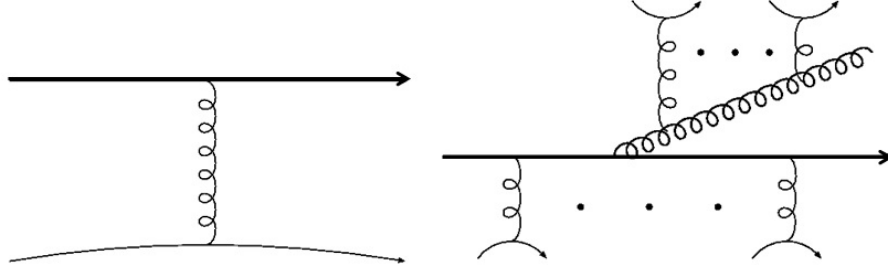


Figure 2.15: The typical diagrams for (left) collisional and (right) radiative energy losses for a parton in a hard scattering as it propagates through the QGP. Taken from [54]

radiative energy loss frameworks that have been developed include: Baier-Dokshitzer-Mueller-Peigne-Schiff-Zakharov (BDMPS-Z) [67], Gyulassy, Levai and Vitev (GLV) [68], Amesto-Salgado-Wiedemann (ASW) [69], Arnold-Moore-Yaffe (AMY) [70] and higher twist (HT) [71].

Both hot and cold nuclear matter effects can be described by modifying Equation 2.14 as:

$$d\sigma_{AB \rightarrow hX} \approx \sum_{abjj'd} f_{a/A}(x_a) \otimes f_{b/B}(x_b) \otimes d\sigma_{ab \rightarrow jd}(\mu_f, \mu_F, \mu_R) \otimes P_{j \rightarrow j'} \otimes D_{h \rightarrow j'}(z_j, \mu_f) \quad (2.16)$$

where the additional  $P_{j \rightarrow j'}$  describes the interaction of the hard parton with the colored medium. This is typically taken as part of the fragmentation modification as:

$$\tilde{D}_{h \rightarrow j'}(z_j, \mu_f) \approx \sum_{j'} P_{j \rightarrow j'}(p_{j'}|p_j) \otimes D_{h \rightarrow j'}(j') \quad (2.17)$$

#### 2.4.1 Jet Reconstruction

Jets can be reconstructed by clustering algorithms that take in a variety of inputs. The algorithm used in ATLAS is the anti- $k_t$  clustering algorithm [72]. This algorithm clusters soft particles around hard ones in the following manner:

- Calculate all distances  $d_{ij}$  between entities  $i$  and  $j$ , and distance  $d_{iB}$  between entity  $i$  and beam  $B$ .
- Identify the smallest distances such that for the smallest distance  $d_{ij}$ , the entities  $i$  and  $j$  are combined

249 and return to beginning.

- 250 • If the smallest distance is  $d_{iB}$ , then take  $i$  as the jet and remove it from the list of entities and return  
251 to beginning.
- 252 • Continue the procedure till the list of items is empty.

253 In general the distance  $d_{ij}$  between the objects is found the via the prescription

$$d_{ij} = \min(k_{Ti}^{2p}, k_{Tj}^{2p}) \frac{\Delta_{ij}^2}{R^2} \quad (2.18)$$

$$d_{iB} = k_{Ti}^{2p} \quad (2.19)$$

254 where  $k_{Ti}$  is the transverse momentum of particle  $i$  and  $\Delta_{ij} = \sqrt{\Delta\eta_{ij}^2 + \Delta\phi_{ij}^2}$  is the distance between  
255 particles  $i$  and  $j$  in  $\eta - \phi$  space.  $R$  the distance parameter and reflects the size of the jet being considered. In the  
256 case of the anti- $k_t$  algorithm,  $p = -1$ . Other popular clustering algorithms like  $k_t$  [73] and Cambridge/Aachen  
257 [74] use  $p = 1$  and  $p = 0$  respectively. The behavior of the different clustering algorithms is shown in  
258 Figure 2.16.

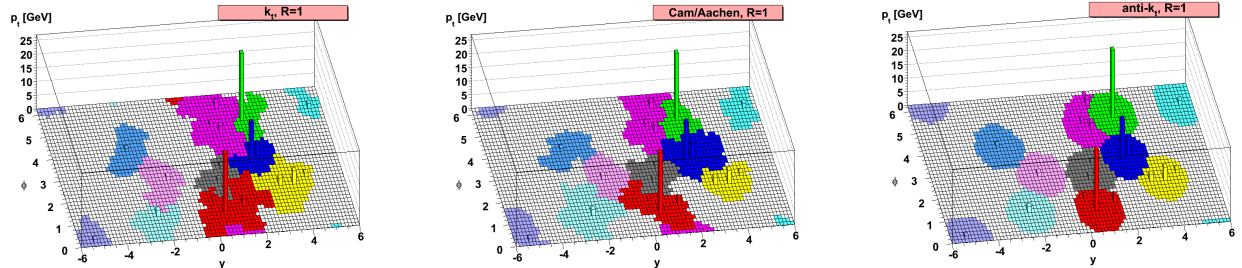


Figure 2.16: Different clustering algorithms applied to the sample parton-level event. Figure taken from [72].

259 The popularity of the anti- $k_t$  algorithm comes from its overcoming of two common problems: collinear  
260 and infrared safety. These are related to instabilities in the cones that are found due to soft radiation.

261 Figure 2.17 describes the collinear safety problem. In a collinear safe jet algorithm, the presence of a virtual  
262 loop or a collinear splitting of a central particle would not change the number of jets being reconstructed.  
263 On the other hand, while a collinear unsafe jet algorithm would not change its output with the presence  
264 of a virtual loop, a splitting in the central particle would lead to the left and right most particles forming  
265 individual seeds, implying two reconstructed jets [75].

266 A schematic describing infrared safety problem is shown in Figure 2.18. Here an infrared safe algorithm  
267 would use the three particles as seeds iteratively find two stable cones. An unsafe algorithm however would

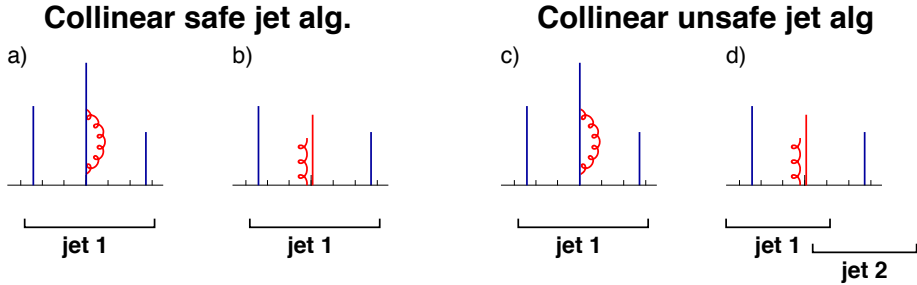


Figure 2.17: An illustration of collinear unsafe behavior. The particle  $p_T$  is proportional to the height and the horizontal axis indicates rapidity. Taken from [75].

268 find three overlapping cones based on the addition of a soft seed.

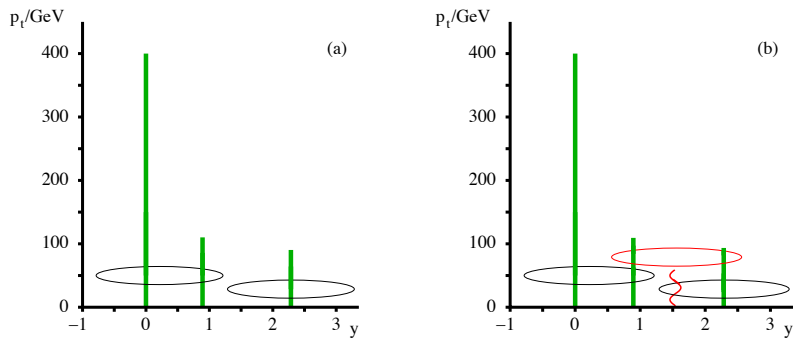


Figure 2.18: An illustration of infrared unsafe behavior. The particle  $p_T$  is proportional to the height and the horizontal axis indicates rapidity. Taken from [76].

269 For heavy ion collisions in ATLAS, the inputs to the algorithm are the  $\eta \times \phi = 0.1 \times 0.1$  calorimeter  
 270 towers. The tower energies are determined by summing up the energies of the individual calorimeter cells.  
 271 The anti- $k_t$  algorithm is first run with the distance parameter  $R = 0.2$ , following which an underlying event  
 272 subtraction procedure is performed. A first estimate of the average underlying event energy density  $\rho_i(\eta)$  is  
 273 done in 0.1 slices of  $\eta$  in each calorimeter layer  $i$  after excluding the regions that overlap with the seed jets.  
 274 A modulation of  $2v_2 \cos[2(\phi - \Psi_2)]$  is applied to account for the flow from the QGP and the underlying event  
 275 is subtracted to give  $E_{Tj}^{\text{sub}}$ :

$$E_{Tj}^{\text{sub}} = E_{Tj} - A_j \rho_i(\eta_j) \left( 1 + 2 \sum_{n=2}^4 v_{ni} (\cos[2(\phi - \Psi_n)]) \right) \quad (2.20)$$

276 where  $E_{Tj}, \eta_j, \phi_j$  and  $A_j$  are the cell  $E_T, \eta, \phi$  and area for cell  $j$  in layer  $i$ . This process is done iteratively  
 277 done one more time after getting new seeds with the distance parameter  $R = 0.2$  and excluding areas that  
 278 are within  $\Delta R = 0.4$  of the seeds. Updated values of  $\rho'_i$  and  $v'_2$  are recalculated and used to estimate the

279 background that is subtracted from the original cell energies. More details on this procedure can be found in  
280 [77].

# Chapter 3

## Major Jet Measurements

281 This chapter shall discuss some important experimental jet measurements that motivate the study of the  
282 main analysis in this thesis. These include the study of the jet yields, dijet asymmetry, and jet fragmentation.  
283 It shall then go on to discuss a few models that have been used to explain the data, looking in particular at  
284 the following: Effective Quenching (EQ), Soft Collinear Effective Theory (SCET), Hybrid Model, and Jet  
285 Fluid Model.

### 286 3.1 Dijet Balance: $x_J$

287 This section will discuss the dijet balance for  $R = 0.4$  jets as measured by ATLAS detector for Pb+Pb  
288 collisions at  $\sqrt{s_{\text{NN}}} = 2.76$  TeV [78]. The dijet imbalance can be expressed in terms of  $x_J$  defined as

$$x_J = \frac{p_{\text{T}2}}{p_{\text{T}1}} \quad (3.1)$$

289 where  $p_{\text{T}2}$  and  $p_{\text{T}1}$  are the transverse momenta of the two highest- $p_{\text{T}}$  jets in the event respectively. The  
290 minimum  $p_{\text{T}2}$  considered is 25 GeV and the pair of jets are separated by  $|\Delta\phi| > 7\pi/8$ . The dijet yields  
291 normalized by the number of jets and determined as  $1/N_{\text{jets}} dN/dx_J$  are presented as a function of  $x_J$  for  
292 different centrality intervals, as well as different ranges for  $p_{\text{T}1}$ . The measured distributions are further  
293 unfolded to remove detector resolution effects and allow comparison to theoretical models.

294 Figure 3.1 shows the  $x_J$  distribution for dijet pairs in  $pp$  and Pb+Pb collisions in two different centrality  
295 bins and two  $p_{\text{T}1}$  ranges. It can be seen that the dijet yields in  $pp$  are peaked at unity and become narrower  
296 for larger  $p_{\text{T}1}$  ranges. This reflects the fact that the effects of jet quenching are minimal and the higher- $p_{\text{T}}$   
297 jets are better balanced. The dijet yields in peripheral Pb+Pb collisions are similar to the distributions from  
298 the  $pp$  data, showing that the effects of quenching are smaller. On the other hand, dijet yields in central  
299 Pb+Pb collisions are significantly broadened, reflecting the maximal of jet quenching. This is consistent with  
300 the picture of the individual jets in the dijet pair traversing different lengths in the QGP and hence losing

301 different amounts of energy. In fact, the distribution for Pb+Pb data is peaked at  $x_J = 0.5$ , implying a loss  
 302 of 50% of the jet  $p_T$ .

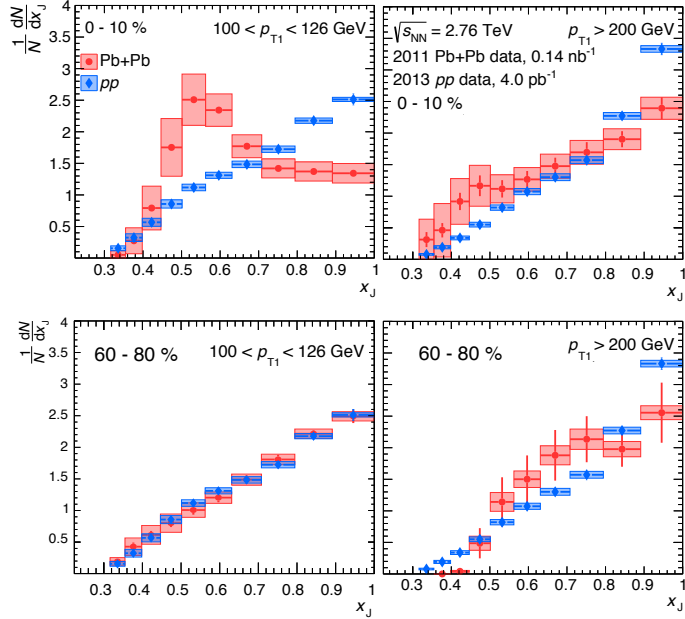


Figure 3.1: The  $1/N_{\text{jets}} dN/dx_J$  distributions for  $R = 0.4$  jets as a function of  $x_J$  for  $pp$  (blue) and  $\text{Pb+Pb}$  (red) collisions. The different panels are for (top) central and (bottom) peripheral collisions in (left)  $100 < p_{T1} < 126 \text{ GeV}$  and (right)  $p_{T1} > 200 \text{ GeV}$ . The  $pp$  data is the same in all panels. The statistical uncertainties are indicated by the bars while the boxes indicate the systematic uncertainties. Figures taken from [78]

303 Further measurements of  $R = 0.3$  jets are shown in Figure 3.2. These distributions are significantly flatter  
 304 than the ones for  $R = 0.4$  jets, an observation that is consistent with the expectation that the transverse  
 305 momenta correlation between the dijet pair is weaker for jets with smaller radii due to radiation that is  
 306 outside the nominal jet cone.

### 307 3.2 Modification of jet yields: $R_{AA}$

308 This section discusses the measurement of the inclusive jet  $R_{AA}$  as measured by the ATLAS detector for  
 309  $R = 0.4$  jets in  $\sqrt{s_{\text{NN}}} = 5.02 \text{ TeV}$   $\text{Pb+Pb}$  collisions [79].

310 While a measurement that compares the jets in a dijet system to each other as discussed in Section 3.1  
 311 can provide valuable information about how jets lose energy, it has the following limitation: If both jets lose  
 312 equal amounts of energy, the dijet yield will still be peaked at unity and no new information will be obtained.  
 313 Thus, it is useful to compare the jet yields directly between the  $pp$  and  $\text{Pb+Pb}$  systems and construct the jet  
 314  $R_{AA}$  observable. This is defined as:

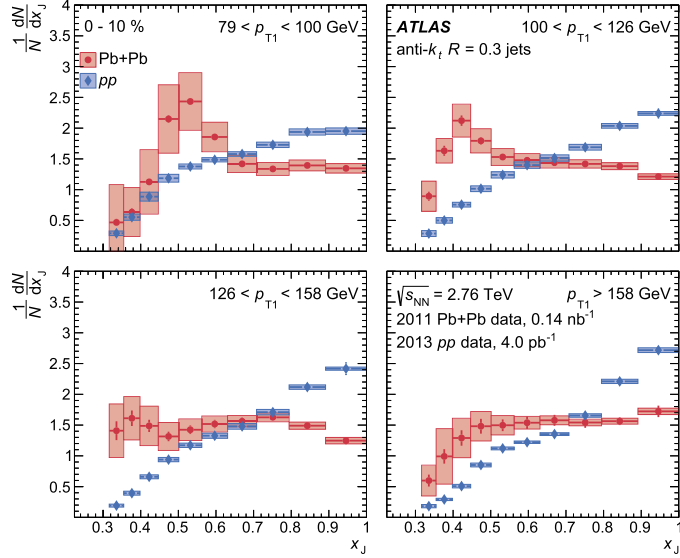


Figure 3.2: The  $1/N_{\text{jets}} dN/dx_J$  distributions for  $R = 0.3$  jets as a function of  $x_J$  in  $pp$  and central  $\text{Pb}+\text{Pb}$  collisions. The different panels are for different,  $p_{\text{T}1}$  ranges (top left to bottom right) central and (bottom) peripheral collisions. The  $\text{Pb}+\text{Pb}$  data is in red circles while the  $pp$  data is in blue diamonds and is the same in all panels. The statistical uncertainties are indicated by the bars while the boxes indicate the systematic uncertainties. Figures taken from [78]

$$R_{\text{AA}} = \frac{\frac{1}{N_{\text{evt}}} \left. \frac{d^2 N_{\text{jet}}}{dp_{\text{T}} dy} \right|_{\text{cent}}}{\langle T_{\text{AA}} \rangle \left. \frac{d^2 \sigma_{\text{jet}}}{dp_{\text{T}} dy} \right|_{\text{pp}}} \quad (3.2)$$

where  $T_{\text{AA}}$  is the nuclear thickness function and accounts for the geometric enhancement between  $pp$  and  $\text{Pb}+\text{Pb}$  as discussed in Section 2.2 and [23].

This measurement was conducted for jets in the 40–1000 GeV range in different rapidity and centrality intervals. The jet yields in  $pp$  and  $\text{Pb}+\text{Pb}$  collisions are shown in Figure 3.3. The  $\text{Pb}+\text{Pb}$  jet yields are scaled by the thickness function and are shown for 8 centrality intervals.

Figure 3.4 shows the measured inclusive jet  $R_{\text{AA}}$  as a function of jet  $p_{\text{T}}$  for different centrality bins and jet rapidity  $|y| < 2.8$ . It can be seen that the most central collisions show a clear suppression with an  $R_{\text{AA}} \approx 0.45$  at jet  $p_{\text{T}} = 100$  GeV. The  $R_{\text{AA}}$  value slowly evolves with jet  $p_{\text{T}}$  and rises to 0.6 at jet  $p_{\text{T}} = 800$  GeV. This modification becomes smaller for more peripheral collisions.

The smooth centrality dependence can be more clearly seen in Figure 3.6(a), where  $R_{\text{AA}}$  is shown as a function of  $\langle N_{\text{part}} \rangle$  for jets in the 100–126 GeV and 200–251 GeV ranges. The magnitude of the suppression is also seen to significantly depend on jet  $p_{\text{T}}$  for  $\langle N_{\text{part}} \rangle \geq 50$ .

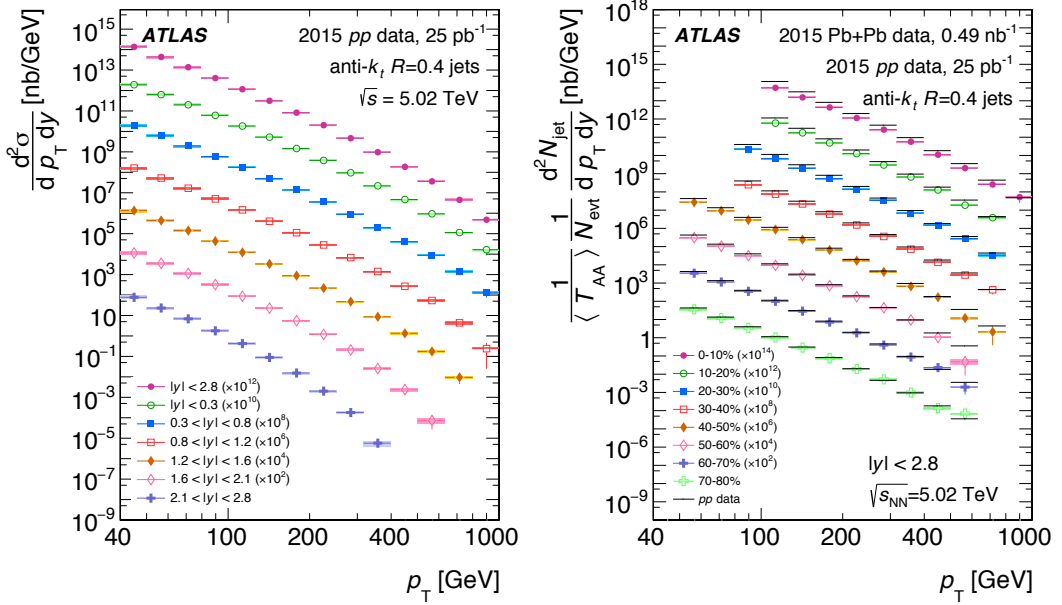


Figure 3.3: (Left) The inclusive jet cross section in  $pp$  collisions as a function of jet  $p_T$  in different  $|y|$  intervals scaled by successive powers of  $10^2$  for visibility. (Right) Per event inclusive jet yield in  $Pb+Pb$  collisions normalized by  $\langle T_{AA} \rangle$  as a function of jet  $p_T$  in different centrality intervals scaled by successive powers of  $10^2$  for visibility. The solid lines represent the cross section from  $pp$  data at the same rapidity interval scaled by the same  $10^2$  factor. Figure taken from [79]

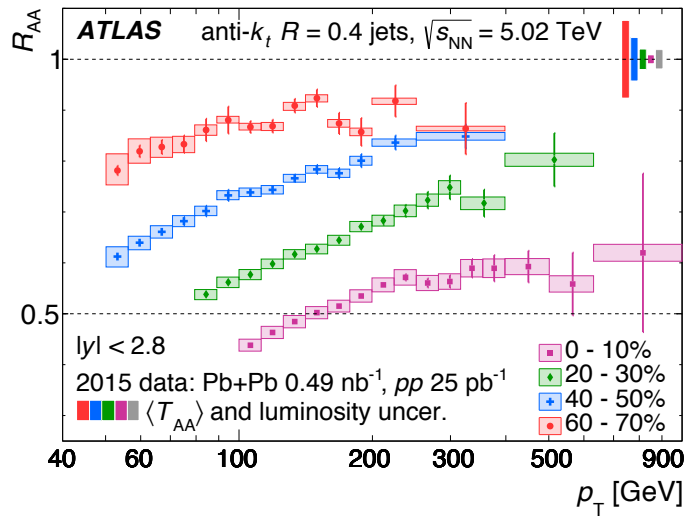


Figure 3.4: The  $R_{AA}$  distributions as a function of jet  $p_T$  for different centrality bins and jet rapidity  $|y| < 2.8$ . The error bars represent statistical uncertainties while the the shaded boxes represent systematic uncertainties. Figure taken from [79]

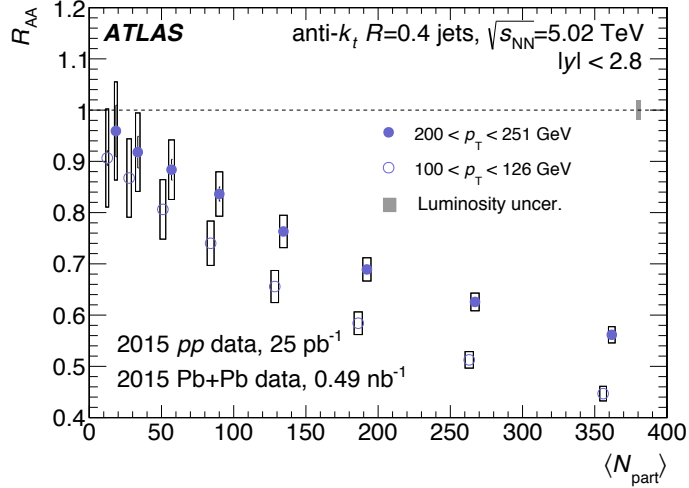


Figure 3.5: The  $R_{AA}$  distributions as a function of jet  $p_T$  for different centrality bins and jet rapidity  $|y| < 2.8$ . The error bars represent statistical uncertainties while the shaded boxes represent systematic uncertainties. Figure taken from [79]

### 327 3.3 Jet Fragmentation

328 [80]

### 329 3.4 Effective Quenching

330 This discussion is based on the model introduced in [81]. This phenomenological model emphasizes the jet  $p_T$   
 331 dependence of the quark to gluon fraction and the difference between quark-jet and gluon-jet quenching. It  
 332 uses an “extended” power law parameterization of the high- $p_T$  hadron spectra coupled with a quenching that  
 333 is based on a non-constant fractional energy loss. This model considers the different color charges carried by  
 334 quarks and gluons and their different splitting functions, and assumes that gluon jets lose energy at a rate  
 335  $9/4$  times higher than quark jets. The key assumption of the model are:

- 336 • The energy lost by a jet is radiated at large angles and does not appear within the jet cone. This is  
 337 backed by [82].
- 338 • The fragmentation pattern of the jet is unaffected by the presence of the QGP i.e. they fragment as  
 339 they would in a vacuum. This is motivated by the idea that the QGP is unable to resolve the internal  
 340 jet structure and is supported by [83, 84].

341 The model uses the following extended power-law parameterization to describe the high- $p_T$  jet spectra:

$$\frac{dn}{dp_T^{\text{jet}}} = A \left( \frac{p_{T0}}{p_T^{\text{jet}}} \right)^{n + \beta \log(p_T^{\text{jet}}/p_{T0})} \quad (3.3)$$

where  $p_{T0}$  is a reference transverse momentum at which  $A = dn/dp_T^{\text{jet}}$ ,  $\beta$  is the logarithmic derivative of  $dn/dp_T^{\text{jet}}$  at  $p_T^{\text{jet}} = p_{T0}$ . Then considering the different quark and gluon fractions as  $f_{q0}$  and  $f_{g0} = 1 - f_{q0}$  respectively, the combined spectrum for quarks and gluons can be written as:

$$\frac{dN}{dp_T^{\text{jet}}} = A \left[ f_{q0} \left( \frac{p_{T0}}{p_T^{\text{jet}}} \right)^{n_q + \beta_q \log(p_T^{\text{jet}}/p_{T0})} + (1 - f_{q0}) \left( \frac{p_{T0}}{p_T^{\text{jet}}} \right)^{n_g + \beta_g \log(p_T^{\text{jet}}/p_{T0})} \right] \quad (3.4)$$

$$f_q(p_T^{\text{jet}}) = \frac{1}{1 + \left( \frac{1 - f_{q0}}{f_{q0}} \right) \left( \frac{p_{T0}}{p_T^{\text{jet}}} \right)^{\Delta n + \Delta \beta \log(p_T^{\text{jet}}/p_{T0})}} \quad (3.5)$$

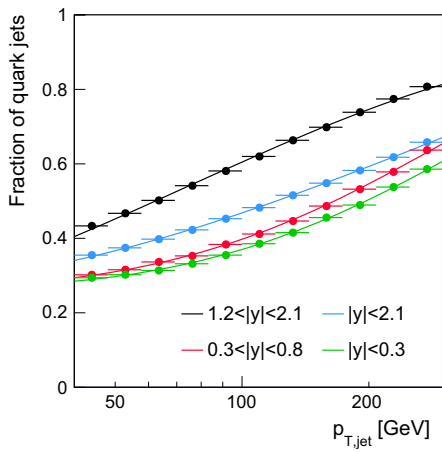
where  $\Delta n = n_g - n_q$  and  $\Delta \beta = \beta_g - \beta_q$ . The  $p_T$  dependence of the quark fraction along with the fit is shown in Figure 3.6(a). The fragmentation functions can also be determined using final-state charged hadrons within a  $R = 0.4$  jet cone. These are fit to the form  $D(z)$ , with fits for the quark and gluon fragmentation shown in Figure 3.6(b).

$$D(z) = a \times \frac{(1 + dz)^b}{(1 + ez)^c} \times e^{-fz} \quad (3.6)$$

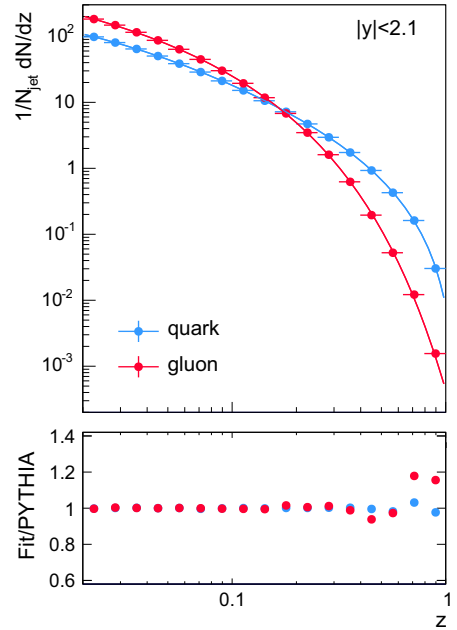
For the quenched spectra, this model assumes a non-constant fractional shift given below as  $S$ . This approach is based on [85] and is used because of the inability of the constant fractional shift to explain the jet  $p_T$  dependence of measured  $R_{\text{AA}}$ .

$$S = s' \left( \frac{p_T^{\text{jet}}}{p_{T0}} \right)^\alpha \quad (3.7)$$

where  $\alpha$  is an undetermined parameter and  $s'$  is the shift for a jet with  $p_T^{\text{jet}} = p_{T0}$ . This gives the following quenched high- $p_T$  hadron spectra:



(a) The jet quark fraction as a function of  $p_T^{\text{jet}}$  in different rapidity bins. The points are from PYTHIA8 simulations and the lines are fits to Equation 3.5.



(b) A comparison of the PYTHIA8 quark and gluon fragmentation. The solid lines are the fits from The jet quark fraction as a function of  $p_T^{\text{jet}}$  in different rapidity bins. The points are from PYTHIA8 simulations and the lines are fits to Equation 3.6.

Figure 3.6: Fits to quark fractions and fragmentation functions from PYTHIA8. Figure taken from [81]

$$\frac{dN_Q}{dp_T^{\text{jet}}} = A \left[ f_{q0} \left( \frac{p_{T0}}{p_T^{\text{jet}} + S_q} \right)^{n_q + \beta_q \log((p_T^{\text{jet}} + S_q)/p_{T0})} \left( 1 + \frac{dS_q}{dp_T^{\text{jet}}} \right) \right. \\ \left. + (1 - f_{q0}) \left( \frac{p_{T0}}{p_T^{\text{jet}} + S_g} \right)^{n_g + \beta_g \log((p_T^{\text{jet}} + S_g)/p_{T0})} \left( 1 + \frac{dS_g}{dp_T^{\text{jet}}} \right) \right] \quad (3.8)$$

354 Where the  $(1 + dS/dp_T^{\text{jet}})$  term is a Jacobian to preserve the number of jets. Then the  $R_{\text{AA}}$  can be written as:

$$R_{\text{AA}} = f_q \left( \frac{1}{1 + S_q/p_T^{\text{jet}}} \right)^{n_q + \beta_q \log((p_T^{\text{jet}} + S_q)/p_{T0})} \frac{p_{T0}}{p_T^{\text{jet}}} \left( 1 + \frac{dS_q}{dp_T^{\text{jet}}} \right) \times \\ (1 - f_q) \left( \frac{1}{1 + S_g/p_T^{\text{jet}}} \right)^{n_g + \beta_g \log((p_T^{\text{jet}} + S_g)/p_{T0})} \frac{p_{T0}}{p_T^{\text{jet}}} \left( 1 + \frac{dS_g}{dp_T^{\text{jet}}} \right) \quad (3.9)$$

(3.10)

355 where the flavor fraction is given by Equation 3.5. These can be fit to the measured ATLAS  $R_{\text{AA}}$  data as  
 356 shown in Figure 3.8(a) and the parameters  $s'$  and  $\alpha$  can be extracted as shown in Figure 3.7.

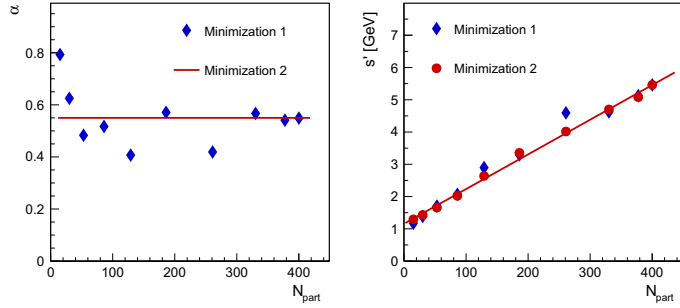
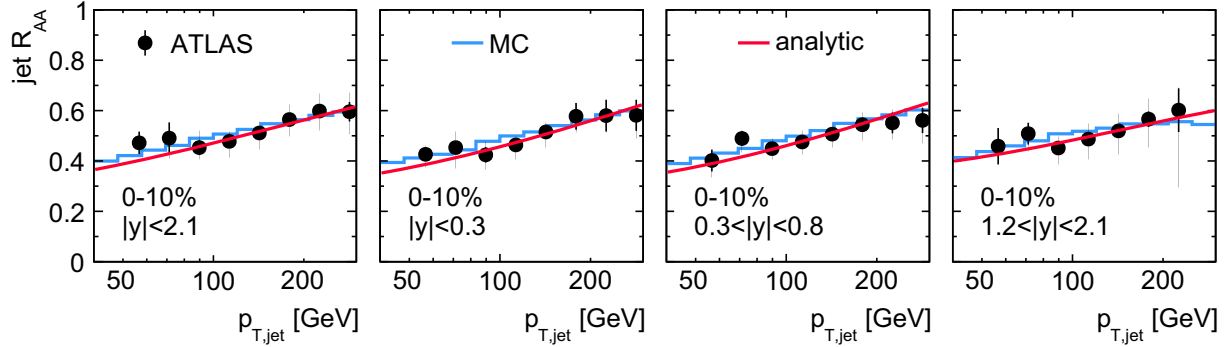
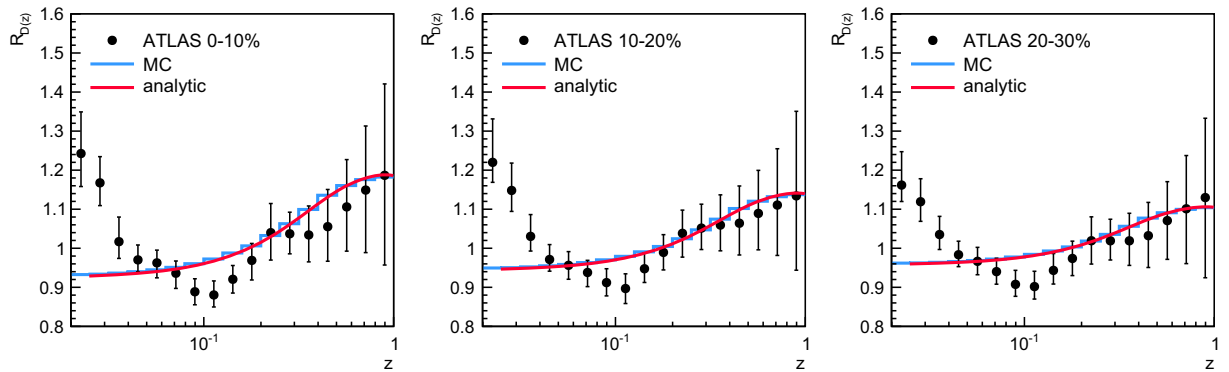


Figure 3.7: The extracted values of  $\alpha$  and  $s'$  as a function of  $N_{\text{part}}$ . The first minimization shows fluctuations for  $\alpha$  around 0.55, which was then fixed for the second minimization to give an  $s'$  that linearly depends on  $N_{\text{part}}$ . Figure taken from [81]

357 It can be seen that the analytic fits and the MC are in good agreement. While the fits agree with the data  
 358 by definition, the robustness of the model can be seen in that it describes the data with a single value for  $\alpha$   
 359 and a simple centrality dependent shift constant  $s'$ . Fits to the  $D(z)$  distributions are shown in Figure 3.8(b)  
 360 and it can be seen that while the MC and analytic calculation agree well with each other, they are only  
 361 able to qualitatively capture some features of the data. The enhancement at high  $z$  can be explained by an  
 362 increased quark content of the jet spectrum and subsequent differential quenching for quark and gluon jets.



(a) A comparison of the  $R_{AA}$  as measured by ATLAS for central Pb+Pb collisions in [86], a MC calculation (blue) and the analytic calculation (red) in the EQ model with the extended power-law parameterization and a non-constant fractional energy loss. The different panels are different rapidity intervals.



(b) A comparison of the  $R_{D(z)}$  as measured by ATLAS in [87], a MC calculation (blue) and the analytic calculation (red) in the EQ model with the extended power-law parameterization and a non-constant fractional energy loss. The different panels are different centrality intervals.

Figure 3.8: A comparison of measured data, MC, and the analytic calculation of the EQ model. Figure taken from [81]

363 The low  $z$  enhancement on the other hand can be considered to be a result of a gluon radiation within the  
 364 jet or a wake from the medium itself.

### 3.5 Jet Fluid model

365 This discussion is based on the model introduced in [88]. This model is based on the evolution of the jet and  
 366 QGP in a coupled manner, considering the energy and transverse momentum exchange between them. In  
 367 this picture, both the jet and medium are allowed to modify each other; the jet is modified via collisional  
 368 and radiative processes while the medium evolves hydrodynamically and is modified because it picks up the  
 369 energy lost by the jet.  
 370

<sup>371</sup> The time evolution of the jet is given

$$f_i(\omega_i, k_{\text{T}i}^2, t) = \frac{dN_i(\omega_i k_{\text{T}i}^2, t)}{d\omega_i dk_{\text{T}i}^2} \quad (3.11)$$

<sup>372</sup> where  $i$  is the type of parton,  $\omega_i$  is its energy, and  $k_{\text{T}}^2$  is its transverse momentum with respect to the jet axis.

<sup>373</sup> Then the transport equations can be written in terms of :

$$\frac{df_j}{dt} = e_j \frac{\partial f_j}{\partial \omega_j} + \frac{1}{4} \hat{q}_j \nabla_{k_{\text{T}}}^2 f_j \quad (3.12)$$

$$+ \sum_i \int d\omega_i dk_{\text{T}i}^2 \frac{d\tilde{\Gamma}_{i \rightarrow j}}{d\omega_j dk_{\text{T}j}^2 dt} f_i \quad (3.13)$$

$$- \sum_i \int d\omega_i dk_{\text{T}i}^2 \frac{d\tilde{\Gamma}_{j \rightarrow i}}{d\omega_i dk_{\text{T}i}^2 dt} f_i \quad (3.14)$$

$$(3.15)$$

<sup>374</sup> where the first term is the collisional energy loss, the second term is the transverse momentum broadening,

<sup>375</sup> and the last two terms are the medium induced gain and loss radiative processes respectively. The splitting

<sup>376</sup> processes are given by:

$$\frac{d\Gamma_{i \rightarrow j}}{d\omega_j dk_{\text{T}j}^2 dt} = \frac{2\alpha_S}{\pi} \hat{q}_g \frac{x P_{i \rightarrow j}(x)}{\omega_j k_{\text{T}j}^4} \sin^2 \left( \frac{t - t_i}{2\tau_f} \right) \quad (3.16)$$

<sup>377</sup> where  $P_{i \rightarrow j}$  is the vacuum splitting function for  $i \rightarrow j$  with  $\omega_j$  being the energy of the radiated parton,  $\tau_f$  is

<sup>378</sup> the formation time of the radiated parton, and  $k_{\text{T}j}$  is the transverse momentum of the radiated parton with

<sup>379</sup> respect to the parent parton. These transport Equations 3.12 can be solved numerically and agree with  $R_{\text{AA}}$

<sup>380</sup> measurements [86, 89, 90]. The effects of the medium are included by considering the energy-momentum

<sup>381</sup> conservation of the jet-QGP system  $\partial_\mu [T_{\text{QGP}}^{\mu\nu} + T_{\text{jet}}^{\mu\nu}] = 0$ . Then the source term  $J^\nu(x)$  that describes the

<sup>382</sup> energy transfer between the jet and the medium can be defined as  $J^\nu(x) \equiv -\partial_\mu T_{\text{jet}}^{\mu\nu}$ , making the QGP

<sup>383</sup> evolution being given by

$$\partial_\mu T_{\text{QGP}}^{\mu\nu} = j^\nu \quad (3.17)$$

384 which characterizes the energy-momentum transfer between the jet and the QGP.

385 An important component of this model is the flow induced by jets. A snapshot of this is shown in  
 386 Figure 3.9, where the evolution of the energy density of the medium can be seen in a sample event. A single  
 387 jet travels through the QGP, and can be clearly seen in the lower panels after the energy of the medium has  
 388 been subtracted out. The V shaped feature seen is the mach cone that is induced by the parton as it moves  
 389 faster than the medium sound velocity.

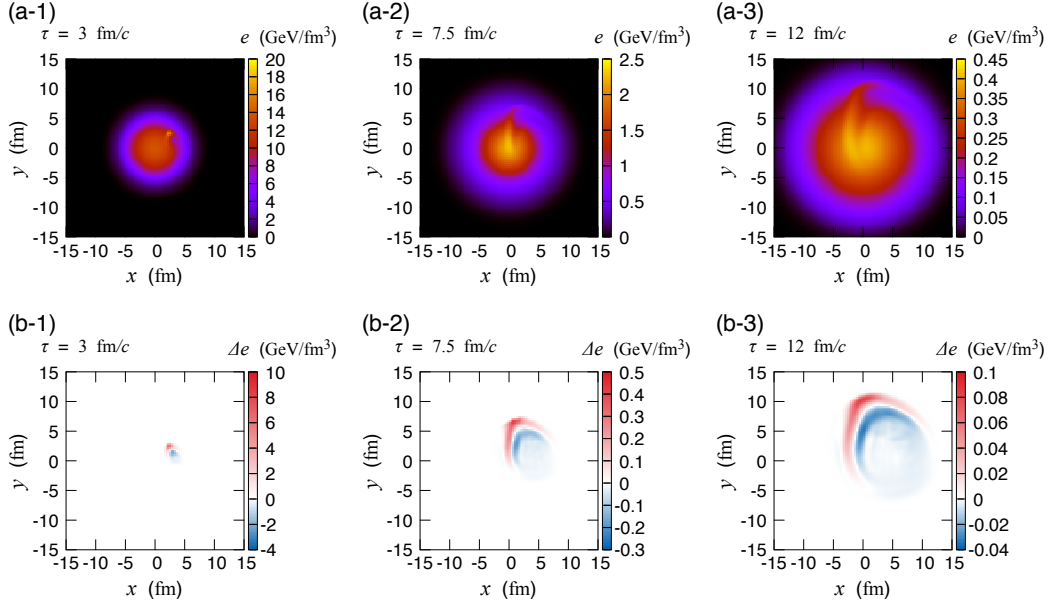


Figure 3.9: (Top) The time evolution of the energy density of the quark gluon plasma with a jet propagating through it. (Bottom) The time evolution of the energy density in the event after the energy density of the QGP has been subtracted out. Figure taken from [88].

390 The final jet energy has two components: the jet shower, and the hydrodynamic response. The former  
 391 as discussed above comprises of the collisional energy loss, momentum broadening, and medium induced  
 392 radiation. The latter includes the energy lost from the jet shower that thermalizes into the medium and  
 393 induces conical flow, some of which is still in the jet cone. This compensates some of the energy lost in the  
 394 shower and can be seen in Figure 3.10. While the absolute amount of energy lost increases as a function of  
 395 initial jet energy, the fractional energy loss decreases. Furthermore there is a cone size dependence once the  
 396 hydrodynamic contributions are included. This is a result of the jet being highly collimated, such that while  
 397 an increase in the size does not change the energy much, it does affect the hydrodynamic contribution from  
 398 the medium.

399 The  $R_{AA}$  distributions constructed with this model and compared to data from CMS [89] are shown in  
 400 Figure 3.11. Including the hydrodynamic contribution decreases the energy loss, hence increasing the  $R_{AA}$

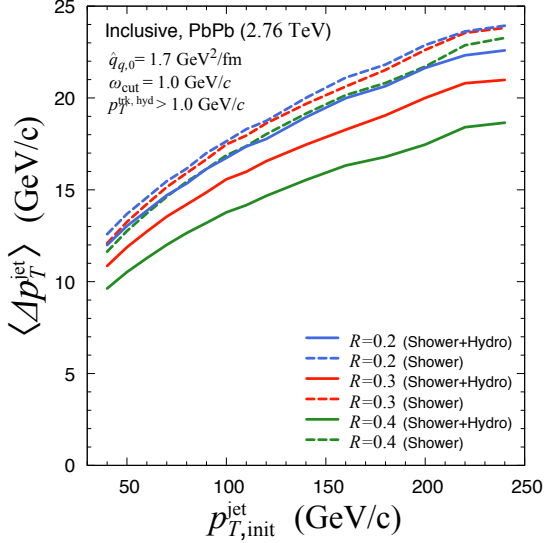


Figure 3.10: (Top) The energy lost by a jets of different radii as a function of their initial energy in central Pb+Pb collisions at  $\sqrt{s_{\text{NN}}} = 2.76 \text{ TeV}$ . Figure taken from [88].

401 value and inducing a cone size dependence to the  $R_{\text{AA}}$ .

402 The internal structure of the jet, i.e. how energy is spread within it, can be investigated using the jet  
403 shape variable, defined as a per-jet quantity as:

$$\rho_{\text{jet}} = \frac{1}{N_{\text{jet}}} \sum_{\text{jet}} \left[ \frac{1}{p_{\text{T}}^{\text{jet}}} \frac{\sum_{\text{trk}} p_{\text{T}}^{\text{ch}}}{\delta r} \right] \quad (3.18)$$

404 where the sum is over all jets and for all tracks around a jet in an annulus with mean radius  $r$  from the jet  
405 axis. The modification in the jet structure then can be defined as:

$$R_{\text{AA}}^\rho = \frac{\rho_{\text{AA}}(r)}{\rho_{\text{pp}}(r)} \quad (3.19)$$

406 A comparison of the jet shape variable  $\rho$  and its modification  $R_{\text{AA}}^\rho$  to data measured by CMS is shown in  
407 Figure 3.12. The individual shower and hydro contributions are seen in Figure 3.12(a). These indicate that  
408 the shower contribution to the jet shape variable falls steeply as a function of distance from the jet axis  
409 while the hydro contribution is fairly constant at large distances. This is because the energy loss from the  
410 shower is carried away by the jet induced flow to large angles. The  $R_{\text{AA}}^\rho$  distribution in Figure 3.12(b), shows  
411 that the core is largely unmodified while the outer part of the jet is broadened. The hydro-contribution

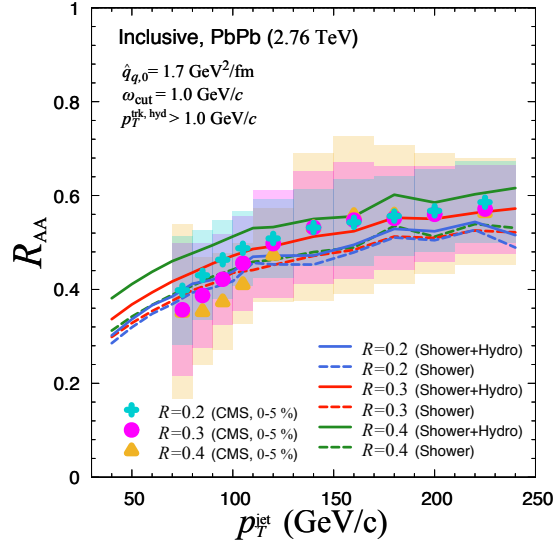
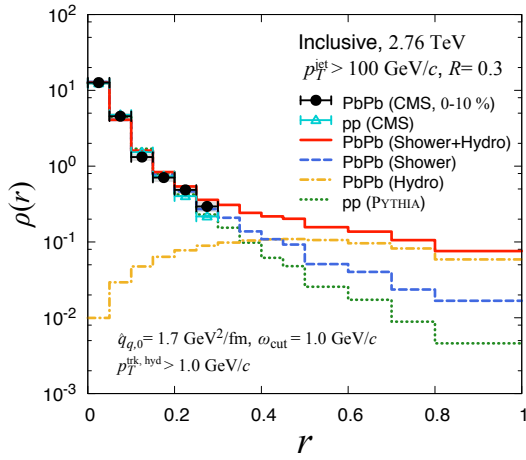


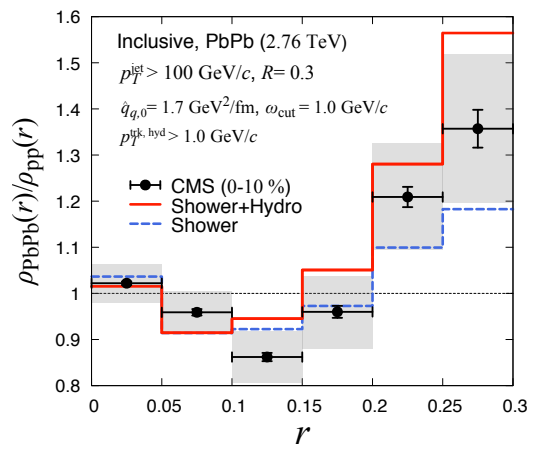
Figure 3.11: The nuclear modification factor  $R_{AA}$  as a function of jet  $p_T$  as determined by the Jet-Fluid model and compared to the data measured by CMS [89]. The different colors represent different sized jets, with the dashed lines showing the modeled  $R_{AA}$  without the hydro-contribution. There is good agreement within the large uncertainties in the data. Figure taken from [88].

<sup>412</sup> mainly has an effect at larger distances from the jet axis. This is consistent with the cone-size dependence  
<sup>413</sup> seen in Figure 3.10.

### <sup>414</sup> 3.6 Hybrid Model



(a) The jet shape as measured by CMS for  $pp$  and central  $Pb+Pb$  collisions [91] compared to the Jet Fluid model. The shower (blue) and hydro (orange) contributions to the jet shape are highlighted.



(b) The modification of the jet shape between  $pp$  and  $Pb+Pb$  as measured by CMS [91] and compared to the Jet Fluid model. The dashed line shows the modeled modification without the hydro-contribution.

Figure 3.12: Fits to CMS data. Figures taken from [88].

# Chapter 4

## Experimental Setup

415 This section will describe the large hadron collider complex and the ATLAS detector and its various subsystems.

### 416 4.1 The Large Hadron Collider

417 The Large Hadron Collider (LHC) is a part of the European Organization for Nuclear Research (CERN).  
418 It has a circumference of 27 kilometers, making it the world's largest particle accelerator, and is housed in  
419 a tunnel that is up to 175 meters below the surface of the earth. The LHC ring has eight arcs and eight  
420 straight sections, with each straight section being approximately 528 m long. Four of the straight sections  
421 are where the major detectors are located, while the other four are used for machine utilities, radio frequency,  
422 collimation and beam dumps. The arc sections are built using 1232 dipole superconducting magnets, providing  
423 a magnetic field of up to 8.33 T. Another 392 quadrupole magnets are used for focussing the particle beam.  
424 Sixteen radio frequency (RF) cavities that provide a voltage of 2 MV and operate at 400 MHz are used to  
425 accelerate the proton or ion beams that are kept in their circular path by the dipole magnets. The magnets  
426 are cooled down to 1.9 K via liquid Helium.

427 The LHC beam pipe has two rings with the counter-rotating beams and uses a uses a twin-bore magnet  
428 design that optimizes for both cost, as well as space. The counterrotating beams require opposite magnetic  
429 dipole fields in both rings, with separate magnetic and vacuum chambers, with the common sections only  
430 at the insertion regions and where the major experimental detectors are located. These detectors are: A  
431 Toroidal LHC Apparatus (ATLAS), Compact Muon Solenoid (CMS), A Large Ion Collider Experiment  
432 (ALICE), and Large Hadron Collider - Beauty (LHCb) [92].

433 Studying the rare events that the LHC was designed for requires high beam energies and intensities, and  
434 the LHC is capable of reaching up to center of mass energies,  $\sqrt{s} = 14$  TeV for protons and  $\sqrt{s_{NN}} = 5.5$   
435 TeV for lead ions. The LHC delivers up to  $10^{34}\text{cm}^2\text{s}^{-1}$  of luminosity to the ATLAS and CMS detectors when  
436 colliding protons. The LHCb detector is a lower luminosity experiment, that receives up to  $10^{32}\text{cm}^2\text{s}^{-1}$ , and  
437 ALICE, a dedicated ion experiment aims at a peak luminosity of  $10^{27}\text{cm}^2\text{s}^{-1}$  for nominal lead-lead operation.

A schematic of the entire accelerator complex and the path followed by protons and heavy ions is shown in Fig. 4.1. The protons in the LHC are obtained by stripping a hydrogen atom of its electrons with an electric field. They are then supplied to the LHC via the Linac2 - Proton Synchrotron Booster - Proton Synchrotron - Super Proton Synchrotron chain. The complete ionization of lead on the other hand is done in multiple stages, with the first stage in Linac3, which provides  $\text{Pb}^{+29}$  via an ion source. The  $\text{Pb}^{+29}$  lead ions are further stripped of electrons by passing them through a  $0.3 \mu\text{m}$  foil. The  $\text{Pb}^{+54}$  ions are selected via mass spectrometer and sent to the Low Energy Ion Ring (LEIR), followed by the Proton Synchrotron and Super Proton Synchrotron, and then finally the LHC. The final stripping of lead ions takes place after the PS, on a  $0.8 \text{ mm}$  thin aluminum foil.

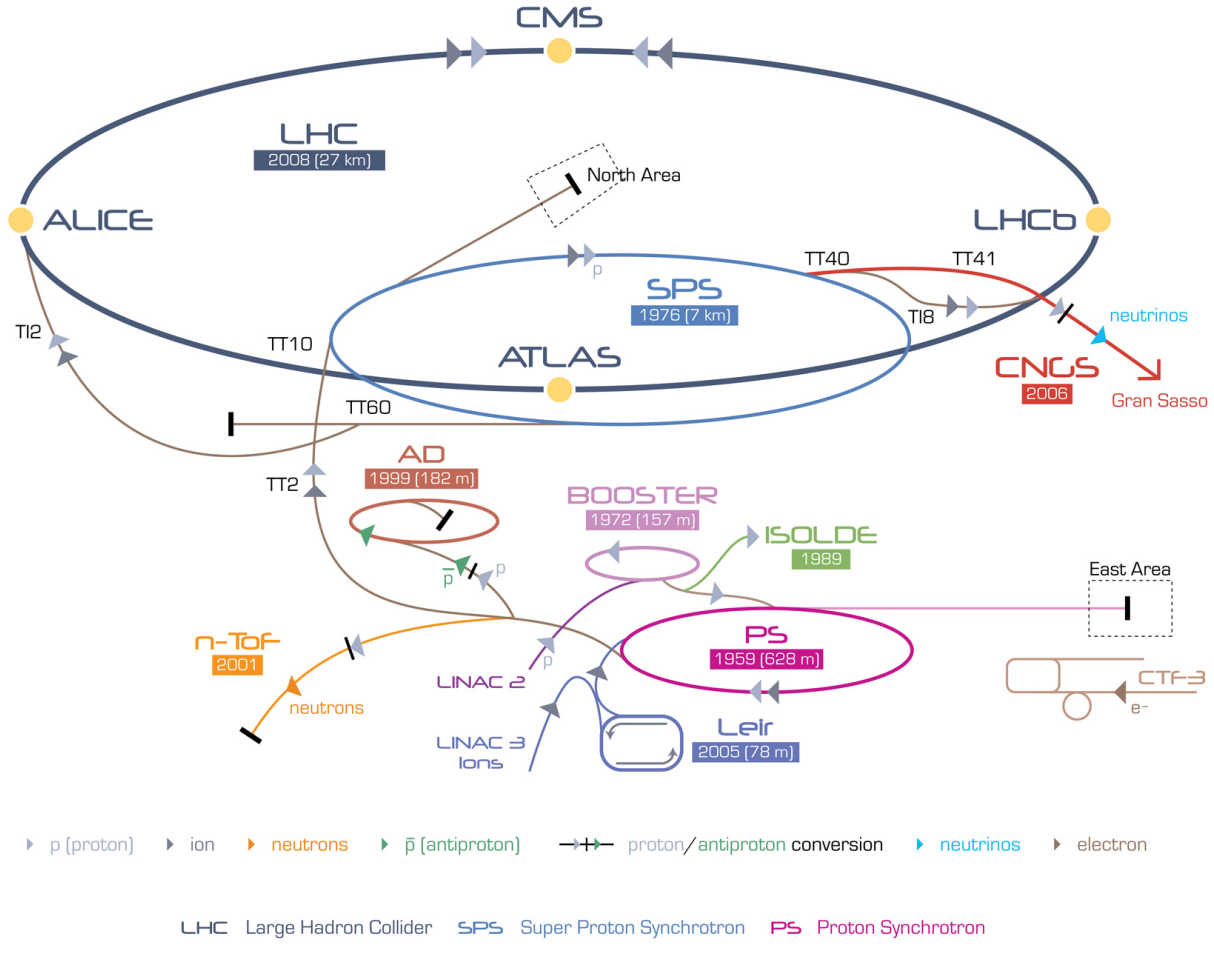


Figure 4.1: The accelerator complex at CERN. ATLAS can be seen inside the SPS on the LHC ring. Figure taken from Ref. [93].

The LHC beams consist of bunches of protons or lead ions with a nominal bunch spacing of 25 ns that corresponds to 2808 bunches.

449 In 2015, the LHC delivered an integrated luminosity of  $0.49 \text{ pb}^{-1}$  of Pb+Pb and  $25 \text{ pb}^{-1}$  of  $pp$  data.

## 450 4.2 The ATLAS Detector

451 The ATLAS detector (Fig. 4.2) is a general purpose detector at the LHC. It uses a right-handed coordinate  
452 system with its origin at the nominal interaction point (IP) in the centre of the detector and the  $z$ -axis  
453 along the beam pipe. The  $x$ -axis points from the IP to the centre of the LHC ring, and the  $y$  axis points  
454 upward. Cylindrical coordinates  $(r, \phi)$  are used in the transverse plane,  $\phi$  being the azimuthal angle around  
455 the beam pipe. The pseudorapidity is defined in terms of the polar angle  $\theta$  as  $\eta = -\ln \tan(\theta/2)$ . The detector  
456 is symmetric in the forward-backward direction, with the positive  $z$  direction being the  $A$  side, and the  
457 negative  $z$  direction being the  $C$  side. It has full  $2\pi$  coverage in azimuth. The transverse momentum  $p_T$ , the  
458 transverse energy  $E_T$ , and the missing transverse energy  $E_{T\text{miss}}$  are defined in the  $x - y$  plane unless stated  
459 otherwise. The distance  $\Delta R$  in the pseudorapidity-azimuthal angle space is defined as  $\Delta R = \sqrt{\Delta\eta^2 + \Delta\phi^2}$ .

460 The detector was designed keeping in mind the goals of the physics it aimed to explore, and as such has  
461 the following characteristics:

- 462 • Fast, radiation-hard electronics and sensor
- 463 • Fine granularity to be able to manage large particle fluxes
- 464 • Large acceptance in pseudorapidity and full azimuthal coverage
- 465 • Good electromagnetic calorimetry for photon and electron identification
- 466 • Good hadron calorimetry for accurate jet and missing transverse energy measurements
- 467 • Good muon identification and momentum resolution
- 468 • Highly efficient trigger system

469 These design goals are achieved with the main subsystems: the inner detector, the calorimeter, the muon  
470 spectrometer, and the trigger system. The main analysis discussed in this thesis uses the inner detector,  
471 calorimeter, and the trigger system. The muon system is described for completeness.

### 472 4.2.1 Inner Detector

473 The inner detector (Fig. 4.3) is designed to reconstruct the charged particle trajectories for particles with  
474 momenta down to 0.5 GeV in the interval  $|\eta| < 2.5$ . It is immersed in a 2T magnetic field from the central

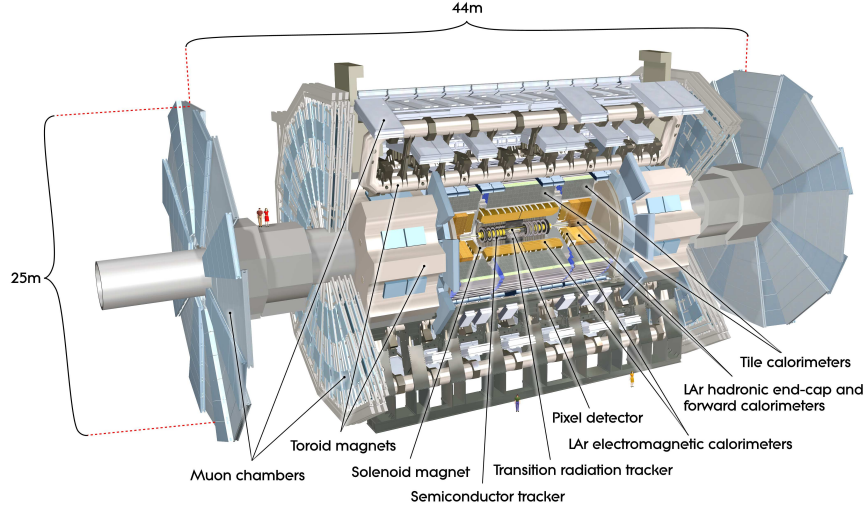


Figure 4.2: The ATLAS detector. Figure taken from Ref. [94].

475 solenoid that covers a region of 5.3 m long and has a diameter of 2.5 m. The inner detector has capabilities for  
 476 pattern recognition, momentum and vertex measurements, and electron identification. These measurements  
 477 are made using the inner pixel detector, the semi-conductor tracker (SCT), and the transition radiation  
 478 tracker (TRT).

479 **Pixel system:** This system is segmented in  $R - \phi$  and comprises of four pixel layers : the innermost  
 480 insertable B layer (IBL) and three identical silicon pixel detectors. The IBL was added to the ATLAS detector  
 481 during the first long shutdown of the LHC in 2013-2014. It consists of 14 carbon fiber staves, 2 cm wide and  
 482 64 cm long, surrounding the beam pipe at a mean radius of 33 mm, and covering a pseudorapidity region of  
 483  $\pm 3$ . Each stave consists of 26880 pixels in a matrix of 80 columns ( $50 \mu\text{m}$  pitch), by 336 rows ( $250 \mu\text{m}$  pitch)  
 484 [95, 96]. The other three layers have a pixel size in  $R - \phi \times z$  of  $50 \times 400 \mu\text{m}^2$ . The accuracies in the  
 485 barrel region are  $10 \mu\text{m}^2 (R - \phi)$  and  $115 \mu\text{m}^2 (z)$ . The end cap regions have an accuracy of  $10 \mu\text{m}^2 (R - \phi)$   
 486 and  $115 \mu\text{m}^2 (R)$ . The hit resolution ranges from  $\sim 8 (R - \phi)$  and  $\sim 40 \mu\text{m} (z)$  for the innermost layer, to  $\sim$   
 487  $10 \mu\text{m} (R - \phi)$  and  $\sim 115 \mu\text{m} (z)$  for the next three layers [94]. The pixel detector has approximately 80.4  
 488 million readout channels.

489 **Semi Conductor Tracker:** This subsystem has a coverage that overlaps with the pixel layers, and  
 490 is arranged in concentric cylinders around the beam axis, with the end caps being disks perpendicular to  
 491 the beam axis. The SCT has eight strip ( $80 \mu\text{m}$  pitch) layers that are crossed by each track. Small angle  
 492 stereo strips (40 mrad) are used to measure both coordinates, with one set of strips in each layer, parallel to  
 493 the beam direction. The end cap region has nine layers of double sided modules with strips in the radial

494 direction, with each also having a mean pitch of  $80\ \mu\text{m}$ . The intrinsic resolution is  $\sim 17\mu\text{m}$  ( $R - \phi$ ) and  $\sim$   
 495  $580\mu\text{m}$  ( $z$ ). There are approximately 6.3 million readout channels from the SCT. [94].

496 **Transition Radiation Tracker:** The TRT uses a combination of a xenon based gas and 4mm diameter  
 497 straw tubes and provides for a large number of hits (up to 36) per track. It covers the region  $|\eta| < 2.0$ , and  
 498 has a resolution of  $\sim 130\mu\text{m}$  in  $r - \phi$ , with no information in the  $z$  direction. The barrel region of the TRT  
 499 has straws that are 144 cm long and are parallel to the beam axis, with the wires divided into two halves at  
 500  $\eta = 0$ . The end-caps have 37 cm long straws in a radial configuration. The TRT has approximately 315,000  
 501 channels. [94].

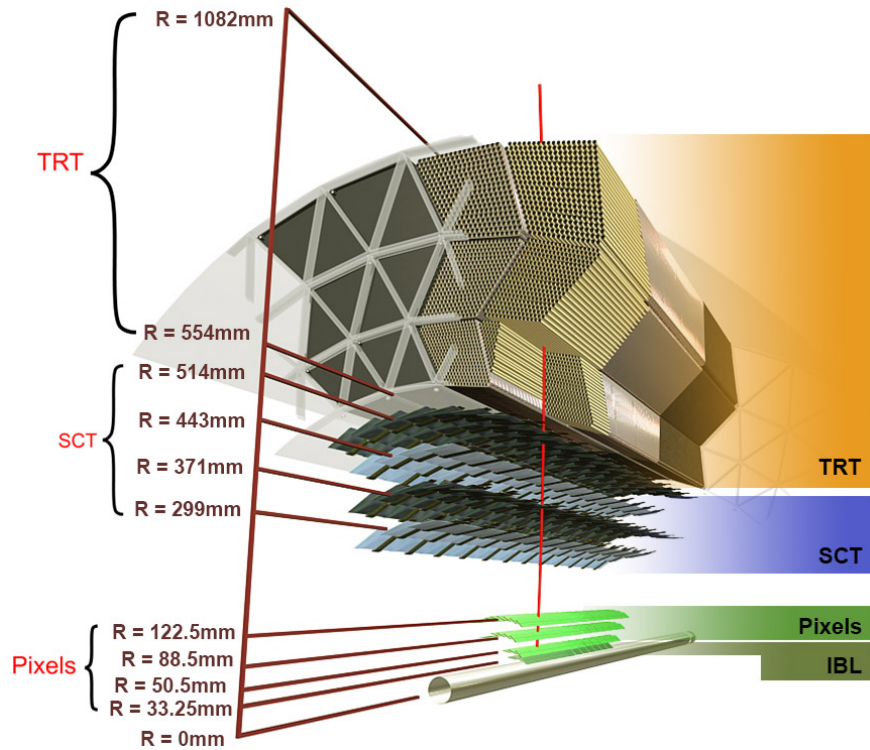


Figure 4.3: ATLAS Inner Detector System

#### 502 4.2.2 Calorimeter

503 The calorimeter covers the range of  $|\eta| < 4.9$  for using a variety of different techniques. The parameters are  
 504 summarized in the table below. Over  $|\eta| < 2.5$ , where there is overlap with the inner detector, the highly  
 505 granular electromagnetic calorimeter is used for precision measurements of electrons and photons. The rest  
 506 of calorimeter has coarser granularity that is sufficient for jet reconstruction. The calorimeter contains the  
 507 electromagnetic and hadronic showers, and limits the punch through to the muon system. The EMCal has a

508 radiation depth greater than 22 radiation lengths in the barrel, and greater than 24 radiation lengths in the  
509 end caps. The approximately 10 interaction lengths in the barrel and end cap provide good resolution for  
510 high energy jets. The total thickness of the calorimeter is 11 interaction lengths at  $\eta = 0$ . The calorimeter is  
511 divided into different subsystems, including the Liquid Argon Electromagnetic Calorimeter (LAr EMCAL)  
512 and the Hadronic calorimeter (HCal).

513 **LAr EMCAL:** The EMCAL covers the region  $|\eta| < 1.475$  and has two end caps ( $1.375 < |\eta| < 3.2$ ). It  
514 also contains the central solenoid. The barrel calorimeter is divided into two half barrels, separated by 4mm  
515 at  $z = 0$ . Each end cap is divided into two coaxial wheels, with the inner one covering  $2.5 < |\eta| < 3.2$  and the  
516 outer one covering  $1.375 < |\eta| < 2.5$ . The EMCAL uses accordion shaped kapton electrodes and lead absorber  
517 plates that provide full azimuthal symmetry. The EMCAL is subdivided into three sections in its depth over  
518  $|\eta| < 2.5$ , the region used for precision physics. The  $|\eta| < 1.8$  region also uses a pre-sampler detector that  
519 uses an active LAr layer to correct for energy lost upstream of the calorimeter. A main source of this loss is  
520 the central solenoid.

521 **Hadronic Calorimeter:** The hadronic calorimeter consists of the tile, LAr Hadronic end cap, and  
522 the LAr forward calorimeter. The tile covers the region  $|\eta| < 1.0$ , with its two barrels covering the range eta  
523  $0.8 < |\eta| < 1.7$ . It uses steel as the absorber and scintillating tiles for the active material. The tile calorimeter  
524 extends radially from an inner radius of 2.28 m to 4.25 m. It has a three layer that are 1.5, 4.1, and 1.8  
525 interaction lengths thick in the barrel region, and 1.5, 2.6, and 3.3 interaction lengths in the extended barrel  
526 region. The total detector thickness is 9.7 interaction lengths at  $\eta = 0$ .

527 The LAr hadronic end cap calorimeter (HEC) consists of two independent wheels per end cap, and is  
528 behind the EMCAL end cap. It extends out from  $1.5 < |\eta| < 3.2$ , and overlaps with the forward calorimeter  
529 and the tile calorimeter. The HEC covers the radial region of 0.475 to 2.03 m.

530 The LAr Forward calorimeter provides coverage over the  $3.1 < |\eta| < 4.9$ . It is approximately 10 interaction  
531 lengths deep, and has three modules, one of which is optimized for electromagnetic measurements, while the  
532 other two for hadronic measurements. Each module is made of concentric rods and tubes parallel to the  
533 beam axis.

534 A summary of the depth of the calorimeter in terms of the interaction lengths, as a function of pseudo-  
535 rapidity is shown in Fig. 4.4.

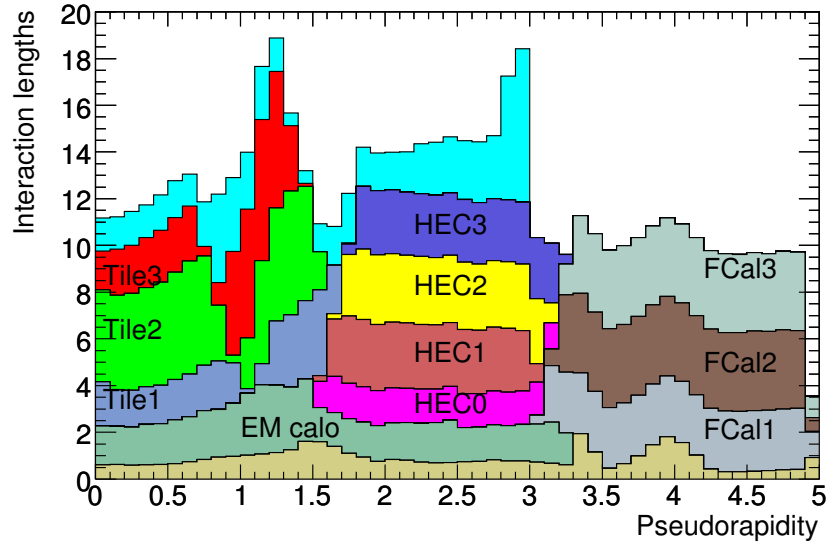


Figure 4.4: Cumulative material in the calorimeter system in units of interaction length as a function of  $|\eta|$ .

### 536 4.2.3 Muon Spectrometer

537 The muon spectrometer is based on the magnetic deflection of muon tracks in the toroid magnets. The  
 538 barrel toroid provides bending over the  $|\eta| < 1.4$  range, and the end cap magnets provide bending in the  
 539  $1.6 < |\eta| < 2.7$  range. In the transition region ( $1.4 < |\eta| < 1.6$ ), the magnetic deflection is from a combination  
 540 of the barrel and end-cap fields. The barrel region has tracks that are measured in chambers in a cylindrical  
 541 configuration around the beam axis. The transition and end-cap have chambers perpendicular to the beam  
 542 axis.

### 543 4.2.4 Other subsystems

544 Other major subsystems of the ATLAS detector include the Zero Degree Calorimeter (ZDC), the trigger  
 545 system

#### 546 ZDC

547 The zero degree calorimeter plays a key role in determining the centrality of heavy ion collisions. It consists of  
 548 quartz rods and tungsten plates, and measures neutral particles at  $|\eta| \geq 8.2$ . It is made of four modules, one  
 549 electromagnetic, and three hadronic. The Modules are made of 11 tungsten plates that are perpendicular to  
 550 the beam direction. Photomultiplier tubes are used to detect the Cherenkov radiation from particle showers.

551 **Trigger System**

552 The trigger and data acquisition system (TDAQ) have different subsystems that are associated with sub-  
 553 detectors. There are three distinct levels: L1, L2, and the event filter. The latter two form the High Level  
 554 Trigger (HLT) system. The L1 trigger, shown in Fig.4.5, uses custom electronics, while the HLT, shown in  
 555 Fig.4.6, is software based. Each level uses information from the previous level to select events.

556 The first level uses limited detector information and makes decisions based on muons, electron, photons,  
 557 jets, and  $\tau$ -leptons carrying a high transverse momentum. It is also capable of identifying large missing and  
 558 total transverse energy. It has a maximum acceptance rate of 75kHz and makes a decision in less than  $2.5\mu s$ .  
 559 This event rate is further reduced to 200 Hz by the HLT that uses the full granularity and precision of the  
 560 inner detector, calorimeter and muon systems to select events.

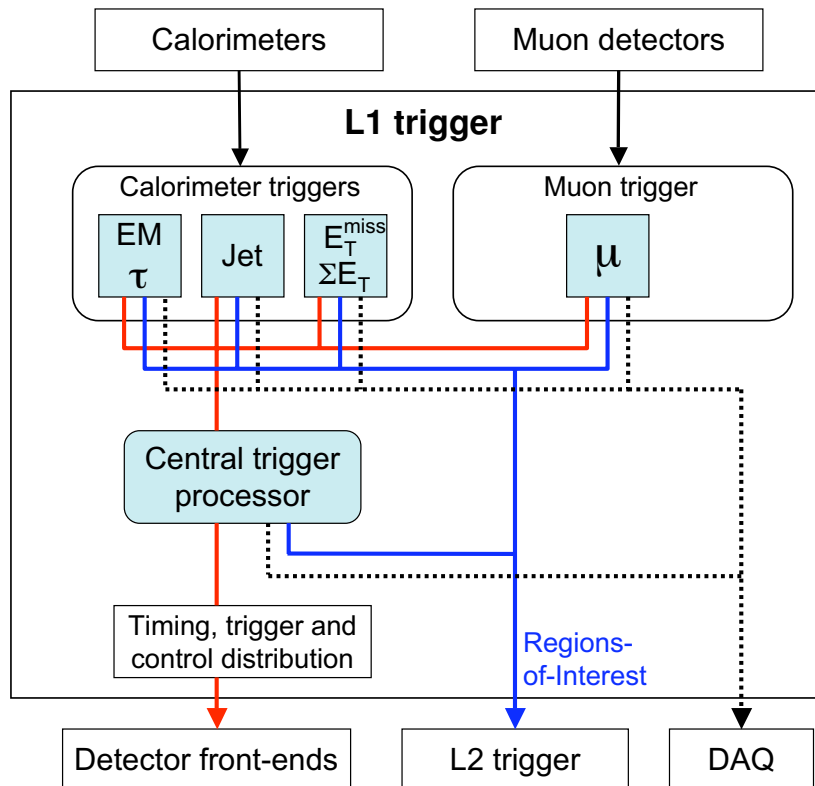


Figure 4.5: Block diagram of the L1 Trigger System.

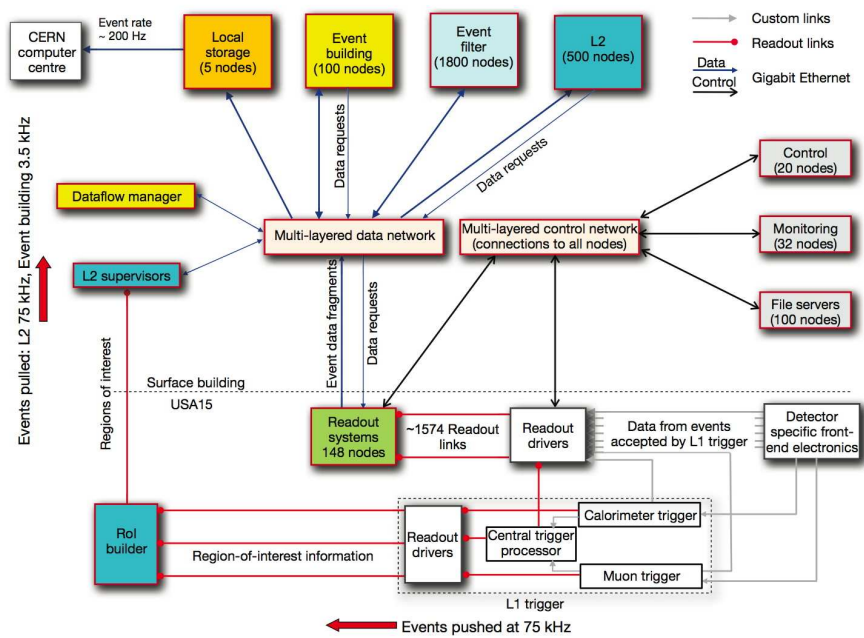


Figure 4.6: Block diagram of the HLT Trigger system.

# Bibliography

- 561 [1] G. Roland, K. Safarik and P. Steinberg, *Heavy-ion collisions at the LHC*, Prog. Part. Nucl. Phys. **77**  
562 (2014) 70 (cit. on p. 1).
- 563 [2] W. Busza et al., *Heavy Ion Collisions: The Big Picture, and the Big Questions*, Ann. Rev. Nucl. Part.  
564 Sci. **68** (2018) 339, arXiv: 1802.04801 [hep-ph] (cit. on pp. 1, 7).
- 565 [3] M. K. Gaillard, P. D. Grannis and F. J. Sciulli, *The Standard model of particle physics*, Rev. Mod.  
566 Phys. **71** (1999) S96, arXiv: hep-ph/9812285 [hep-ph] (cit. on p. 3).
- 567 [4] J Beringer et al., *Review of Particle Physics, 2012-2013. Review of Particle Properties*, Phys. Rev. D  
568 **86** (2012) 010001 (cit. on pp. 4, 5).
- 569 [5] A. Deur et al., *High precision determination of the  $Q^2$  evolution of the Bjorken Sum*, Phys. Rev. **D90**  
570 (2014) 012009, arXiv: 1405.7854 [nucl-ex] (cit. on p. 6).
- 571 [6] J. H. Kim et al., *A Measurement of  $\alpha_s(Q^2)$  from the Gross-Llewellyn Smith sum rule*, Phys. Rev. Lett.  
572 **81** (1998) 3595, arXiv: hep-ex/9808015 [hep-ex] (cit. on p. 6).
- 573 [7] G. Altarelli et al., *Determination of the Bjorken sum and strong coupling from polarized structure  
574 functions*, Nucl. Phys. **B496** (1997) 337, arXiv: hep-ph/9701289 [hep-ph] (cit. on p. 6).
- 575 [8] H. W. Kendall, *Deep inelastic scattering: Experiments on the proton and the observation of scaling*,  
576 Rev. Mod. Phys. **63** (3 1991) 597 (cit. on p. 6).
- 577 [9] A. L. Kataev, G. Parente and A. V. Sidorov, *Improved fits to the  $xF_3$  CCFR data at the next-to-next-to-  
578 leading order and beyond*, Phys. Part. Nucl. **34** (2003) 20, [Erratum: Phys. Part. Nucl.38,no.6,827(2007)],  
579 arXiv: hep-ph/0106221 [hep-ph] (cit. on p. 6).
- 580 [10] S. Alekhin, J. Blumlein and S. Moch, *Parton Distribution Functions and Benchmark Cross Sections at  
581 NNLO*, Phys. Rev. **D86** (2012) 054009, arXiv: 1202.2281 [hep-ph] (cit. on p. 6).
- 582 [11] S. Alekhin, J. Blumlein and S.-O. Moch, *ABM news and benchmarks*, PoS **DIS2013** (2013) 039, arXiv:  
583 1308.5166 [hep-ph] (cit. on p. 6).

- 584 [12] J. Blumlein, H. Bottcher and A. Guffanti, *Non-singlet QCD analysis of deep inelastic world data at*  
 585  $O(\alpha_s^3)$ , Nucl. Phys. **B774** (2007) 182, arXiv: [hep-ph/0607200 \[hep-ph\]](#) (cit. on p. 6).
- 586 [13] H1 Collaboration, *Three- and Four-jet Production at Low  $x$  at HERA*, Eur. Phys. J. **C54** (2008) 389,  
 587 arXiv: [0711.2606 \[hep-ex\]](#) (cit. on p. 6).
- 588 [14] ZEUS Collaboration, *Forward-jet production in deep inelastic ep scattering at HERA*, Eur. Phys. J.  
 589 **C52** (2007) 515, arXiv: [0707.3093 \[hep-ex\]](#) (cit. on p. 6).
- 590 [15] ZEUS Collaboration, *Multi-jet cross-sections in charged current  $e^\pm p$  scattering at HERA*, Phys. Rev.  
 591 **D78** (2008) 032004, arXiv: [0802.3955 \[hep-ex\]](#) (cit. on p. 6).
- 592 [16] ZEUS Collaboration, *Inclusive dijet cross sections in neutral current deep inelastic scattering at HERA*,  
 593 Eur. Phys. J. **C70** (2010) 965, arXiv: [1010.6167 \[hep-ex\]](#) (cit. on p. 6).
- 594 [17] ZEUS Collaboration, *Inclusive-jet cross sections in NC DIS at HERA and a comparison of the  $kT$ ,*  
 595 *anti- $kT$  and SIScone jet algorithms*, Phys. Lett. **B691** (2010) 127, arXiv: [1003.2923 \[hep-ex\]](#) (cit. on  
 596 p. 6).
- 597 [18] H1 Collaboration, *Jet Production in ep Collisions at High  $Q^2$  and Determination of  $\alpha_s$* , Eur. Phys. J.  
 598 **C65** (2010) 363, arXiv: [0904.3870 \[hep-ex\]](#) (cit. on p. 6).
- 599 [19] E. V. Shuryak, *Quantum chromodynamics and the theory of superdense matter*, Physics Reports **61**  
 600 (1980) 71 , ISSN: 0370-1573 (cit. on pp. 6, 11).
- 601 [20] R. Glauber, *Lectures in theoretical physics*, ed. WE Brittin and LG Dunham, Interscience, New York **1**  
 602 (1959) 315 (cit. on p. 7).
- 603 [21] R. Glauber et al., *Lectures in theoretical physics*, 1959 (cit. on p. 7).
- 604 [22] H. D. Vries, C. D. Jager and C. D. Vries, *Nuclear charge-density-distribution parameters from elastic*  
 605 *electron scattering*, Atomic Data and Nuclear Data Tables **36** (1987) 495 , ISSN: 0092-640X (cit. on  
 606 pp. 7, 8).
- 607 [23] M. L. Miller, K. Reygers, S. J. Sanders and P. Steinberg, *Glauber Modeling in High-Energy Nuclear*  
 608 *Collisions*, Annual Review of Nuclear and Particle Science **57** (2007) 205 (cit. on pp. 7, 8, 10, 23).
- 609 [24] B. Alver, M. Baker, C. Loizides and P. Steinberg, *The PHOBOS Glauber Monte Carlo*, (2008), arXiv:  
 610 [0805.4411 \[nucl-ex\]](#) (cit. on p. 7).
- 611 [25] D. Kharzeev and M. Nardi, *Hadron production in nuclear collisions at RHIC and high density QCD*,  
 612 Phys. Lett. **B507** (2001) 121, arXiv: [nucl-th/0012025 \[nucl-th\]](#) (cit. on p. 9).

- 613 [26] A. Bialas, M. Bleszynski and W. Czyz, *Multiplicity Distributions in Nucleus-Nucleus Collisions at*  
 614 *High-Energies*, Nucl. Phys. **B111** (1976) 461 (cit. on p. 9).
- 615 [27] ATLAS Collaboration, *Centrality determination in  $\sqrt{s_{NN}} = 5.02 \text{ TeV Pb+Pb collision data in 2015}$* ,  
 616 tech. rep. ATL-COM-PHYS-2016-1287, CERN, 2016 (cit. on p. 10).
- 617 [28] J. C. Collins and M. J. Perry, *Superdense Matter: Neutrons or Asymptotically Free Quarks?*, Phys. Rev.  
 618 Lett. **34** (21 1975) 1353 (cit. on p. 11).
- 619 [29] A. D. Linde, *Phase transitions in gauge theories and cosmology*, Reports on Progress in Physics **42**  
 620 (1979) 389 (cit. on p. 11).
- 621 [30] S. B. Ruster, V. Werth, M. Buballa, I. A. Shovkovy and D. H. Rischke, *Phase diagram of neutral quark*  
 622 *matter: Self-consistent treatment of quark masses*, Phys. Rev. D **72** (3 2005) 034004 (cit. on p. 11).
- 623 [31] PHENIX Collaboration, *Enhanced Production of Direct Photons in Au + Au Collisions at  $\sqrt{s_{NN}} =$*   
 624 *200 GeV and Implications for the Initial Temperature*, Phys. Rev. Lett. **104** (13 2010) 132301 (cit. on  
 625 p. 11).
- 626 [32] ALICE Collaboration, *Direct photon production in Pb-Pb collisions at sNN=2.76 TeV*, Physics Letters  
 627 B **754** (2016) 235 , ISSN: 0370-2693 (cit. on p. 11).
- 628 [33] Z. Fodor and S. Katz, *Critical point of QCD at finite T and  $\lambda$ , lattice results for physical quark masses*,  
 629 *Journal of High Energy Physics* **2004** (2004) 050 (cit. on p. 11).
- 630 [34] STAR Collaboration, *Experimental and theoretical challenges in the search for the quark-gluon plasma: The STAR Collaboration's critical assessment of the evidence from RHIC collisions*, Nuclear Physics A  
 631 **757** (2005) 102 , First Three Years of Operation of RHIC, ISSN: 0375-9474 (cit. on p. 11).
- 633 [35] ALICE Collaboration, *Production of light nuclei and anti-nuclei in pp and Pb-Pb collisions at energies available at the CERN Large Hadron Collider*, Phys. Rev. C **93** (2 2016) 024917 (cit. on p. 11).
- 635 [36] PHENIX Collaboration, *Single identified hadron spectra from  $\sqrt{s_{NN}} = 130 \text{ GeV Au + Au collisions}$* ,  
 636 Phys. Rev. C **69** (2 2004) 024904 (cit. on p. 11).
- 637 [37] BRAHMS Collaboration, *Centrality dependent particle production at  $y = 0$  and  $y \geq 1$  in Au+Au collisions at  $\sqrt{s_{NN}} = 200 \text{ GeV}$* , Phys. Rev. C **72** (1 2005) 014908 (cit. on p. 11).
- 639 [38] PHOBOS Collaboration, *Identified hadron transverse momentum spectra in Au+Au collisions at  $\sqrt{s_{NN}} = 62.4 \text{ GeV}$* , Phys. Rev. C **75** (2 2007) 024910 (cit. on p. 11).
- 641 [39] ALICE Collaboration, *Centrality dependence of  $\pi$ ,  $K$ , and  $p$  production in Pb-Pb collisions at  $\sqrt{s_{NN}} =$*   
 642 *2.76 TeV*, Phys. Rev. C **88** (4 2013) 044910 (cit. on p. 11).

- 643 [40] ATLAS Collaboration, *Measurement of the azimuthal anisotropy of charged particles produced in  $\sqrt{s_{NN}} =$*   
 644 *5.02 TeV Pb+Pb collisions with the ATLAS detector*, *Eur. Phys. J.* **C78** (2018) 997, arXiv: [1808.03951](#)  
 645 [[nucl-ex](#)] (cit. on p. 12).
- 646 [41] PHENIX Collaboration, *Elliptic Flow of Identified Hadrons in Au + Au Collisions at  $\sqrt{s_{NN}} = 200$*   
 647 *GeV*, *Phys. Rev. Lett.* **91** (18 2003) 182301 (cit. on p. 12).
- 648 [42] CMS Collaboration, *Non-Gaussian elliptic-flow fluctuations in PbPb collisions at  $\sqrt{s_{NN}} = 5.02$  TeV*,  
 649 *Phys. Lett.* **B789** (2019) 643, arXiv: [1711.05594](#) [[nucl-ex](#)] (cit. on p. 12).
- 650 [43] ALICE Collaboration, *Anisotropic Flow of Charged Particles in Pb-Pb Collisions at  $\sqrt{s_{NN}} = 5.02$  TeV*,  
 651 *Phys. Rev. Lett.* **116** (13 2016) 132302 (cit. on p. 12).
- 652 [44] M. Connors, C. Nattrass, R. Reed and S. Salur, *Jet measurements in heavy ion physics*, *Rev. Mod.*  
 653 *Phys.* **90** (2 2018) 025005 (cit. on p. 12).
- 654 [45] A. M. Poskanzer and S. A. Voloshin, *Methods for analyzing anisotropic flow in relativistic nuclear*  
 655 *collisions*, *Phys. Rev.* **C58** (1998) 1671, arXiv: [nucl-ex/9805001](#) [[nucl-ex](#)] (cit. on p. 12).
- 656 [46] U. Heinz and R. Snellings, *Collective flow and viscosity in relativistic heavy-ion collisions*, *Ann. Rev.*  
 657 *Nucl. Part. Sci.* **63** (2013) 123, arXiv: [1301.2826](#) [[nucl-th](#)] (cit. on p. 12).
- 658 [47] H. Niemi, K. J. Eskola and R. Paatelainen, *Event-by-event fluctuations in a perturbative QCD +*  
 659 *saturation + hydrodynamics model: Determining QCD matter shear viscosity in ultrarelativistic heavy-*  
 660 *ion collisions*, *Phys. Rev.* **C93** (2016) 024907, arXiv: [1505.02677](#) [[hep-ph](#)] (cit. on p. 13).
- 661 [48] ALICE Collaboration, *Higher harmonic anisotropic flow measurements of charged particles in Pb-Pb*  
 662 *collisions at  $\sqrt{s_{NN}} = 2.76$  TeV*, *Phys. Rev. Lett.* **107** (2011) 032301, arXiv: [1105.3865](#) [[nucl-ex](#)]  
 663 (cit. on p. 13).
- 664 [49] J. D. Bjorken, *Highly relativistic nucleus-nucleus collisions: The central rapidity region*, *Phys. Rev. D*  
 665 **27** (1 1983) 140 (cit. on p. 12).
- 666 [50] PHENIX Collaboration, *Formation of dense partonic matter in relativistic nucleus-nucleus collisions at*  
 667 *RHIC: Experimental evaluation by the PHENIX collaboration*, *Nucl. Phys.* **A757** (2005) 184, arXiv:  
 668 [nucl-ex/0410003](#) [[nucl-ex](#)] (cit. on p. 13).
- 669 [51] CMS Collaboration, *Charged hadron multiplicity and transverse energy densities in PbPb collisions*  
 670 *from CMS*, *Journal of Physics G: Nuclear and Particle Physics* **38** (2011) 124041 (cit. on p. 13).
- 671 [52] B. Muller, J. Schukraft and B. Wyslouch, *First Results from Pb+Pb collisions at the LHC*, *Ann. Rev.*  
 672 *Nucl. Part. Sci.* **62** (2012) 361, arXiv: [1202.3233](#) [[hep-ex](#)] (cit. on p. 14).

- 673 [53] T. Sjostrand, S. Mrenna and P. Z. Skands, *A Brief Introduction to PYTHIA 8.1*, *Comput. Phys. Commun.* **178** (2008) 852, arXiv: [0710.3820 \[hep-ph\]](#) (cit. on p. 13).
- 674 [54] G.-Y. Qin and X.-N. Wang, *Jet quenching in high-energy heavy-ion collisions*, *Int. J. Mod. Phys. E* **24** (2015) 1530014, [,309(2016)], arXiv: [1511.00790 \[hep-ph\]](#) [hep-ph] (cit. on pp. 13, 14, 17).
- 675 [55] A. D. Martin, W. J. Stirling, R. S. Thorne and G. Watt, *Parton distributions for the LHC*, *The European Physical Journal C* **63** (2009) 189, ISSN: 1434-6052, URL: <https://doi.org/10.1140/epjc/s10052-009-1072-5> (cit. on p. 15).
- 676 [56] M. Hirai, S. Kumano and T.-H. Nagai, *Determination of nuclear parton distribution functions and their uncertainties at next-to-leading order*, *Phys. Rev. C* **76** (6 2007) 065207 (cit. on p. 16).
- 677 [57] D. de Florian and R. Sassot, *Nuclear parton distributions at next to leading order*, *Phys. Rev. D* **69** (7 2004) 074028 (cit. on p. 16).
- 678 [58] K. Eskola, H Paukkunen and C. Salgado, *EPS09 — A new generation of NLO and LO nuclear parton distribution functions*, *Journal of High Energy Physics* **2009** (2009) 065 (cit. on p. 16).
- 679 [59] S. J. Brodsky and H. J. Lu, *Shadowing and antishadowing of nuclear structure functions*, *Phys. Rev. Lett.* **64** (12 1990) 1342 (cit. on p. 16).
- 680 [60] European Muon Collaboration, *The ratio of the nucleon structure functions F2N for iron and deuterium*, *Physics Letters B* **123** (1983) 275 , ISSN: 0370-2693 (cit. on p. 16).
- 681 [61] O. Hen, E. Piasetzky and L. B. Weinstein, *New data strengthen the connection between short range correlations and the EMC effect*, *Phys. Rev. C* **85** (4 2012) 047301 (cit. on p. 16).
- 682 [62] K. Saito and T. Uchiyama, *Effect of the Fermi Motion on Nuclear Structure Functions and the Emc Effect*, *Z. Phys. A* **322** (1985) 299 (cit. on p. 16).
- 683 [63] CMS Collaboration, *Jet momentum dependence of jet quenching in PbPb collisions at sNN=2.76 TeV*, *Physics Letters B* **712** (2012) 176 , ISSN: 0370-2693 (cit. on p. 16).
- 684 [64] ATLAS collaboration, *Study of inclusive jet yields in Pb+Pb collisions at  $\sqrt{s_{NN}} = 5.02$  TeV*, (2017) (cit. on p. 16).
- 685 [65] The CMS collaboration, *Measurement of transverse momentum relative to dijet systems in PbPb and pp collisions at  $\sqrt{s_{NN}} = 2.76$  TeV*, *Journal of High Energy Physics* **2016** (2016) 6, ISSN: 1029-8479, URL: [https://doi.org/10.1007/JHEP01\(2016\)006](https://doi.org/10.1007/JHEP01(2016)006) (cit. on p. 16).
- 686 [66] S. Chatrchyan et al., *Jet momentum dependence of jet quenching in PbPb collisions at  $\sqrt{s_{NN}} = 2.76$  TeV*, *Phys. Lett. B* **712** (2012) 176, arXiv: [1202.5022 \[nucl-ex\]](#) (cit. on p. 16).

- 703 [67] R. Baier, Y. Dokshitzer, A. Mueller, S. Peigné and D. Schiff, *Radiative energy loss of high energy quarks*  
 704 *and gluons in a finite-volume quark-gluon plasma*, Nuclear Physics B **483** (1997) 291 , ISSN: 0550-3213  
 705 (cit. on p. 17).
- 706 [68] M. Gyulassy, P. Levai and I. Vitev, *Jet quenching in thin quark gluon plasmas. 1. Formalism*, Nucl.  
 707 Phys. **B571** (2000) 197, arXiv: [hep-ph/9907461 \[hep-ph\]](#) (cit. on p. 17).
- 708 [69] U. A. Wiedemann, *Gluon radiation off hard quarks in a nuclear environment: Opacity expansion*, Nucl.  
 709 Phys. **B588** (2000) 303, arXiv: [hep-ph/0005129 \[hep-ph\]](#) (cit. on p. 17).
- 710 [70] P. B. Arnold, G. D. Moore and L. G. Yaffe, *Photon emission from ultrarelativistic plasmas*, JHEP **11**  
 711 (2001) 057, arXiv: [hep-ph/0109064 \[hep-ph\]](#) (cit. on p. 17).
- 712 [71] X.-F. Guo and X.-N. Wang, *Multiple scattering, parton energy loss and modified fragmentation functions*  
 713 *in deeply inelastic e A scattering*, Phys. Rev. Lett. **85** (2000) 3591, arXiv: [hep-ph/0005044 \[hep-ph\]](#)  
 714 (cit. on p. 17).
- 715 [72] M. Cacciari, G. P. Salam and G. Soyez, *The Anti- $k(t)$  jet clustering algorithm*, JHEP **0804** (2008) 063,  
 716 arXiv: [0802.1189 \[hep-ph\]](#) (cit. on pp. 17, 18).
- 717 [73] S. Catani, Y. L. Dokshitzer, M. H. Seymour and B. R. Webber, *Longitudinally invariant  $K_t$  clustering*  
 718 *algorithms for hadron hadron collisions*, Nucl. Phys. **B406** (1993) 187 (cit. on p. 18).
- 719 [74] Y. L. Dokshitzer, G. D. Leder, S. Moretti and B. R. Webber, *Better jet clustering algorithms*, JHEP  
 720 **08** (1997) 001, arXiv: [hep-ph/9707323 \[hep-ph\]](#) (cit. on p. 18).
- 721 [75] G. P. Salam, *Towards Jetography*, Eur. Phys. J. **C67** (2010) 637, arXiv: [0906.1833 \[hep-ph\]](#) (cit. on  
 722 pp. 18, 19).
- 723 [76] G. P. Salam and G. Soyez, *A practical seedless infrared-safe cone jet algorithm*, Journal of High Energy  
 724 Physics **2007** (2007) 086 (cit. on p. 19).
- 725 [77] ATLAS Collaboration, *Measurement of the jet radius and transverse momentum dependence of inclusive*  
 726 *jet suppression in lead-lead collisions at  $\sqrt{s_{NN}} = 2.76$  TeV with the ATLAS detector*, Phys. Lett. **B719**  
 727 (2013) 220, arXiv: [1208.1967 \[hep-ex\]](#) (cit. on p. 20).
- 728 [78] ATLAS Collaboration, *Measurement of jet  $p_T$  correlations in Pb+Pb and pp collisions at  $\sqrt{s_{NN}} = 2.76$*   
 729 *TeV with the ATLAS detector*, Phys. Lett. **B774** (2017) 379, arXiv: [1706.09363 \[hep-ex\]](#) (cit. on  
 730 pp. 21–23).

- 731 [79] ATLAS Collaboration, *Measurement of the nuclear modification factor for inclusive jets in Pb+Pb*  
 732 *collisions at  $\sqrt{s_{NN}} = 5.02 \text{ TeV}$  with the ATLAS detector*, *Phys. Lett.* **B790** (2019) 108, arXiv: [1805.05635 \[nucl-ex\]](#) (cit. on pp. 22, 24, 25).
- 734 [80] ATLAS Collaboration, *Measurement of jet fragmentation in Pb+Pb and pp collisions at  $\sqrt{s_{NN}} = 5.02$*   
 735 *TeV with the ATLAS detector*, *Phys. Rev.* **C98** (2018) 024908, arXiv: [1805.05424 \[nucl-ex\]](#) (cit. on  
 736 p. 25).
- 737 [81] M. Spousta and B. Cole, *Interpreting single jet measurements in Pb + Pb collisions at the LHC*, *Eur.*  
 738 *Phys. J. C* **76** (2016) 50, arXiv: [1504.05169 \[hep-ph\]](#) (cit. on pp. 25, 27–29).
- 739 [82] CMS Collaboration, *Observation and studies of jet quenching in PbPb collisions at nucleon-nucleon*  
 740 *center-of-mass energy = 2.76 TeV*, *Phys. Rev.* **C84** (2011) 024906, arXiv: [1102.1957 \[nucl-ex\]](#)  
 741 (cit. on p. 25).
- 742 [83] J.-P. Blaizot, E. Iancu and Y. Mehtar-Tani, *Medium-induced QCD cascade: democratic branching and*  
 743 *wave turbulence*, *Phys. Rev. Lett.* **111** (2013) 052001, arXiv: [1301.6102 \[hep-ph\]](#) (cit. on p. 25).
- 744 [84] J. Casalderrey-Solana, Y. Mehtar-Tani, C. A. Salgado and K. Tywoniuk, *New picture of jet quenching*  
 745 *dictated by color coherence*, *Phys. Lett.* **B725** (2013) 357, arXiv: [1210.7765 \[hep-ph\]](#) (cit. on p. 25).
- 746 [85] R. Baier, Y. L. Dokshitzer, A. H. Mueller and D. Schiff, *Quenching of hadron spectra in media*, *JHEP*  
 747 **09** (2001) 033, arXiv: [hep-ph/0106347 \[hep-ph\]](#) (cit. on p. 26).
- 748 [86] ATLAS Collaboration, *Measurements of the Nuclear Modification Factor for Jets in Pb+Pb Collisions*  
 749 *at  $\sqrt{s_{NN}} = 2.76 \text{ TeV}$  with the ATLAS Detector*, *Phys. Rev. Lett.* **114** (2015) 072302, arXiv: [1411.2357](#)  
 750 [\[hep-ex\]](#) (cit. on pp. 29, 30).
- 751 [87] ATLAS Collaboration, *Measurement of inclusive jet charged-particle fragmentation functions in Pb+Pb*  
 752 *collisions at  $\sqrt{s_{NN}} = 2.76 \text{ TeV}$  with the ATLAS detector*, *Phys. Lett. B* **739** (2014) 320, arXiv:  
 753 [1406.2979 \[hep-ex\]](#) [\[hep-ex\]](#) (cit. on p. 29).
- 754 [88] Y. Tachibana, N.-B. Chang and G.-Y. Qin, *Full jet in quark-gluon plasma with hydrodynamic medium*  
 755 *response*, *Phys. Rev.* **C95** (2017) 044909, arXiv: [1701.07951 \[nucl-th\]](#) (cit. on pp. 29, 31–34).
- 756 [89] CMS Collaboration, *Measurement of inclusive jet cross sections in pp and PbPb collisions at  $\sqrt{s_{NN}} =$*   
 757 *2.76 TeV*, *Phys. Rev. C* **96** (2017) 015202, arXiv: [1609.05383 \[nucl-ex\]](#) (cit. on pp. 30, 31, 33).
- 758 [90] ALICE Collaboration, *Measurement of charged jet suppression in Pb-Pb collisions at  $\sqrt{s_{NN}} = 2.76$*   
 759 *TeV*, *JHEP* **03** (2014) 013, arXiv: [1311.0633 \[nucl-ex\]](#) (cit. on p. 30).

- 760 [91] CMS Collaboration, *Modification of jet shapes in PbPb collisions at  $\sqrt{s_{NN}} = 2.76 \text{ TeV}$* , *Phys. Lett.*  
761 **B730** (2014) 243, arXiv: [1310.0878\[nucl-ex\]](https://arxiv.org/abs/1310.0878) [[nucl-ex](#)] (cit. on p. 34).
- 762 [92] L. Evans and P. Bryant, *LHC Machine*, *Journal of Instrumentation* **3** (2008) S08001 (cit. on p. 35).
- 763 [93] C. Lefevre, ‘The CERN accelerator complex’, 2008 (cit. on p. 36).
- 764 [94] ATLAS Collaboration, *The ATLAS Experiment at the CERN Large Hadron Collider*, *JINST* **3** (2008)  
765 S08003 (cit. on pp. 38, 39).
- 766 [95] A. La Rosa, *The ATLAS Insertable B-Layer: from construction to operation*, *JINST* **11** (2016) C12036,  
767 arXiv: [1610.01994 \[physics.ins-det\]](https://arxiv.org/abs/1610.01994) (cit. on p. 38).
- 768 [96] ATLAS Collaboration, *ATLAS Insertable B-Layer Technical Design Report*, tech. rep., 2010 (cit. on  
769 p. 38).